

SELECTED SCIENCE HIGHLIGHTS FROM THE FIRST 5 YEARS OF THE UPPER ATMOSPHERE RESEARCH SATELLITE (UARS) PROGRAM

A. E. Dessler,¹ M. D. Burrage,² J.-U. Grooss,³
J. R. Holton,⁴ J. L. Lean,⁵ S. T. Massie,⁶
M. R. Schoeberl,⁷ A. R. Douglass,⁷
and C. H. Jackman⁷

Abstract. We present scientific highlights from the Upper Atmosphere Research Satellite (UARS) program obtained during the first 5 years of the program. The UARS measures the chemical composition and meteorological state of the middle and upper atmosphere as well as the solar irradiance. The comprehensive suite of UARS geophysical parameters, their near-global coverage, and the multiyear time span have

yielded new insights into the processes affecting our atmosphere. In this article we select seven scientific issues, including stratospheric ozone chemistry, the dynamics of the middle and upper atmosphere, and solar irradiance variations, and discuss the significant impact that the UARS observations have had on our understanding of each issue.

1. INTRODUCTION

NASA officially announced its intent to develop the Upper Atmosphere Research Satellite (UARS) in 1979. Nine instruments and a science team were then chosen by an open proposal selection process. An additional instrument, the Active Cavity Radiometer Irradiance Monitor (ACRIM), was given a flight of opportunity on the UARS spacecraft. These 10 instruments are listed and a brief description of their capabilities is given in Table 1. The UARS, considered the first of the Mission to Planet Earth series of NASA spacecraft, was originally scheduled to be launched in the mid-1980s. Funding deferment and the *Challenger* accident, however, delayed the deployment until September 15, 1991.

The suite of instruments aboard the UARS allows scientists to address issues covering the altitude range

from 12 km to well above 100 km, encompassing parts of or all of the troposphere, stratosphere, mesosphere, and thermosphere. The troposphere is the lowest 10–15 km of the atmosphere and is characterized by decreasing temperature with increasing altitude. The troposphere contains ~90% of the mass of the atmosphere as well as most of the Earth's clouds and weather. The layer above the troposphere is the stratosphere, which is characterized by increasing temperature with altitude and contains the vast majority of the atmosphere's ozone. The temperature minimum between these layers is called the tropopause. Another temperature maximum near 50 km (~1 hPa), called the stratopause, marks the boundary between the stratosphere and the layer above it, the mesosphere. In the mesosphere the temperature again decreases with altitude. The top of the mesosphere is defined by a temperature minimum called the mesopause. Above the mesopause sits the thermosphere.

By mid-1996, nearly 400 peer-reviewed articles had utilized UARS data. Each of the 10 instruments has produced high-quality data as well as important scientific results. Early scientific results from UARS were published in two special issues of widely read journals: *Geophysical Research Letters*, 20(12), 1993, and the *Journal of the Atmospheric Sciences*, 51(20), 1994. Detailed descriptions of the UARS instruments can be found in a special issue of the *Journal of Geophysical Research*, 98(D6), 1993. Validation reports for the various UARS data products can be found in another special issue of the *Journal of Geophysical Research*, 101(D6), 1996.

¹Department of Meteorology, University of Maryland, College Park.

²Space Physics Research Laboratory, Department of Atmospheric, Oceanic, and Space Sciences, University of Michigan, Ann Arbor.

³Forschungszentrum Jülich, Jülich, Germany.

⁴Department of Atmospheric Sciences, University of Washington, Seattle.

⁵Naval Research Laboratory, Washington, D. C.

⁶National Center for Atmospheric Research, Boulder, Colorado.

⁷Laboratory for Atmospheres, NASA Goddard Space Flight Center, Greenbelt, Maryland.

TABLE 1. Scientific Payload of the UARS

| <i>Instrument</i> | <i>Technique</i> | <i>Measurement</i> | <i>Investigator</i> |
|---|--|--|--|
| SOLSTICE (Solar-Stellar Irradiance Comparison Experiment) | full-disk solar irradiance spectrometer incorporating stellar comparisons for onboard sensitivity tracking | solar UV spectral (1 nm) irradiance from 420 to 120 nm | G. J. Rottman, University of Colorado |
| SUSIM (Solar Ultraviolet Spectral Irradiance Monitor) | full-disk solar irradiance spectrometer incorporating onboard sensitivity tracking using D ₂ lamps and redundant optical elements | solar UV spectral (1 nm) irradiance from 410 to 120 nm | G. E. Brueckner, Naval Research Laboratory |
| ACRIM (Active Cavity Radiometer Irradiance Monitor) | full-disk solar total irradiance cavity radiometers | solar total (spectrally integrated) irradiance | R. C. Willson, Columbia University |
| PEM (Particle Environment Monitor) | X ray, proton, and electron spectrometers | energetic particle flux, X ray flux, and magnetic field | J. D. Winningham, Southwest Research Institute |
| CLAES (Cryogenic Limb Array Etalon Spectrometer) | solid-cryogen cooled interferometer sensing atmospheric infrared emissions | T, O ₃ , ClONO ₂ , N ₂ O, CH ₄ , N ₂ O ₅ , HNO ₃ , H ₂ O, CFCl ₃ , CF ₂ Cl ₂ , aerosols | A. E. Roche, Lockheed Palo Alto Research Laboratory |
| ISAMS (Improved Stratospheric and Mesospheric Sounder) | mechanically cooled radiometer sensing atmospheric infrared emissions | T, O ₃ , CO, HNO ₃ , NO, NO ₂ , N ₂ O, H ₂ O, N ₂ O ₅ , HNO ₃ | F. W. Taylor, University of Oxford, England |
| HALOE (Halogen Occultation Experiment) | gas filter/radiometer sensing atmospheric absorption of sunlight | T, O ₃ , HCl, HF, NO, NO ₂ , CH ₄ , H ₂ O, aerosol | J. M. Russell III, Hampton University |
| MLS (Microwave Limb Sounder) | microwave radiometer | T, O ₃ , ClO, H ₂ O, SO ₂ , HNO ₃ | J. W. Waters, Jet Propulsion Laboratory |
| HRDI (High-Resolution Doppler Imager) | Fabry-Perot spectrometer sensing atmospheric emission scattering and absorption | mesospheric winds, O ₃ , T, and stratospheric winds | P. B. Hays, University of Michigan |
| WINDII (Wind Imaging Interferometer Sounder) | Michelson interferometer sensing atmospheric airglow emission | mesospheric winds | G. G. Shepherd, York University |

Adapted from *Reber* [1993].

With few exceptions, the UARS data are publicly available (see the appendix).

It would be impossible to present a comprehensive review of the scientific advances of the UARS within the confines of any article. Instead, this review presents a cross section of highlights of the UARS program that illustrate both the breadth and utility of the data set. Selecting these highlights was both difficult and subjective. In the end, it was decided to pattern this paper after the presentations made in the session “Upper Atmosphere Research Satellite (UARS) Science Highlights” (session U01) at the 1995 American Geophysical Union Fall Meeting.

Section 2 describes some operational details of the satellite. The remainder of the paper is organized roughly by scientific discipline. Sections 3 through 5 deal with stratospheric chemistry. Section 3 presents a review of lower and middle stratospheric chlorine partitioning as measured by UARS. The partitioning of chlorine atoms among the molecules HCl, ClONO₂, and ClO is a critical factor in determining the effects of man on lower and middle stratospheric ozone loss. Section 4 presents a review of UARS contributions to our knowledge of upper stratospheric ozone production and loss processes. Section 5 discusses some important contributions

by UARS to our knowledge of aerosols and polar stratospheric clouds (PSCs). These particles serve as sites for chemical reactions that are crucial for regulating ozone.

Section 6 reviews UARS analyses of the interaction between chemistry and transport in the northern hemisphere polar region. This section shows that while an “ozone hole” has not formed in the Arctic, loss of ozone has been occurring each winter as a result of mechanisms similar to those that create the Antarctic ozone hole. Sections 7 and 8 focus on UARS contributions to our understanding of the dynamics of the atmosphere. Section 7 presents an analysis of UARS trace constituent measurements and their implications for stratospheric transport processes. Section 8 discusses direct wind measurements in the stratosphere and mesosphere.

Finally, section 9 presents an overview of the UARS solar total and ultraviolet (UV) spectral irradiance measurements. Sunlight is the major energy input for the Earth, and as such it controls the climate and the rate of important photochemical reactions. Changes of solar irradiance therefore can have an unparalleled impact on our atmosphere, making long-term measurements of solar irradiance critical. Section 10 presents conclusions.

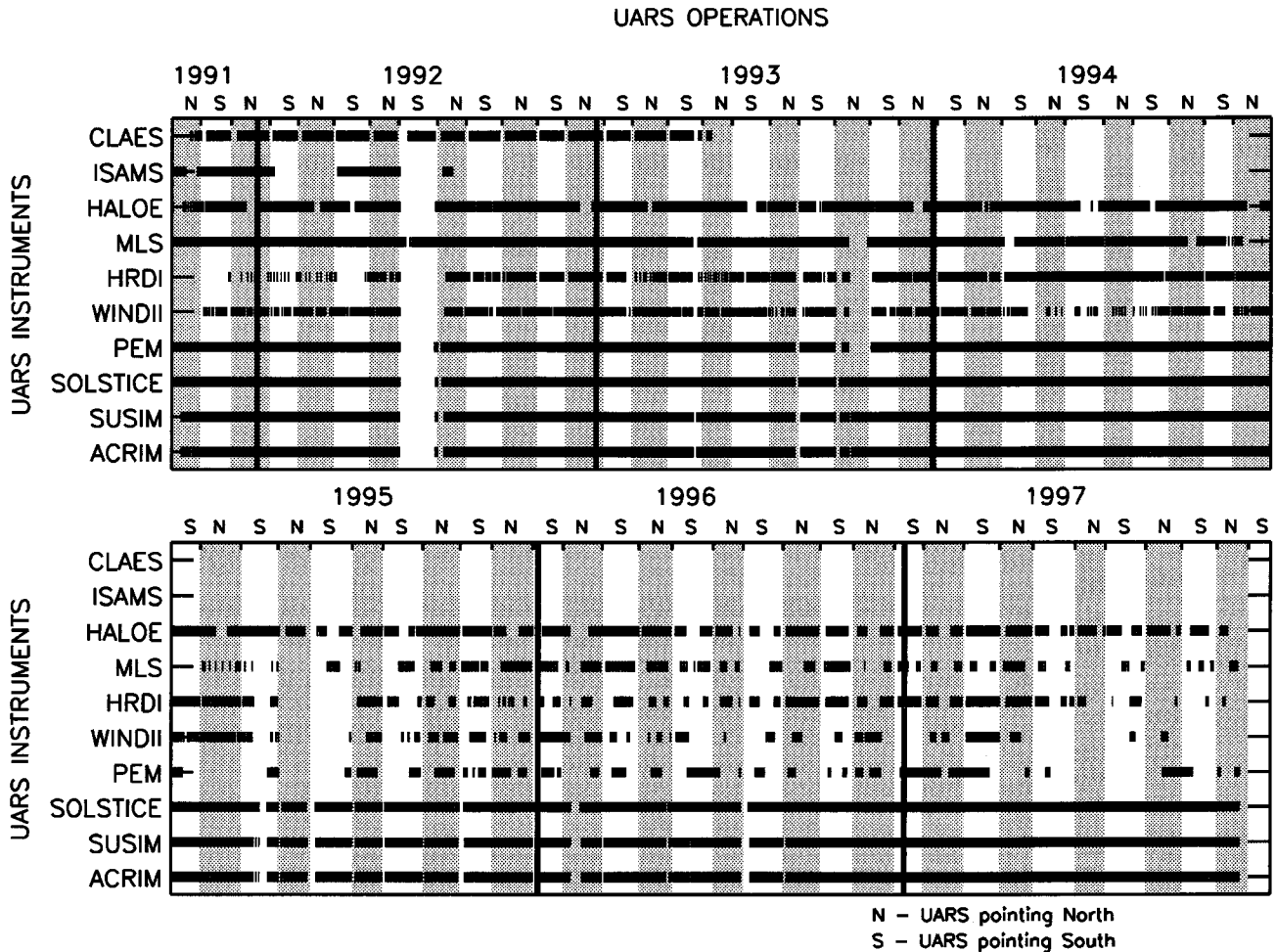


Figure 1. Time series of instrument operational status. Black signifies that the instrument is taking data. The N and S on the top axis of the plot indicate whether the MLS, CLAES, WINDII, and HRDI instruments were looking at the northern or southern hemisphere.

2. SATELLITE OVERVIEW

Most instruments are mounted on the side of the satellite that faces away from the Sun (the “cold side” of the satellite) to better control their temperature. Because of the precession of the 57° inclination orbit, without intervention the cold side of the spacecraft would become exposed to direct sunlight within about a month. To prevent this, every ~ 36 days the UARS is rotated by 180° . This has a significant impact on the sampling pattern of the limb-sounding instruments MLS, CLAES, WINDII, and HRDI (see Table 1 for the definitions of these acronyms). During a north “yaw cycle” the latitude coverage of these instruments is from 32°S to 80°N latitude. After ~ 36 days, the satellite rotates or “yaws” for a south cycle, with the limb-scanning instruments viewing from 80°S to 32°N latitude. ISAMS is equipped with two telescopes and thus was able to view from both sides of the spacecraft. The solar instruments are mounted on a gimballed platform that independently tracks the Sun. HALOE, mounted on the

warm side of the spacecraft, also has a separate tracking telescope.

Figure 1 shows the times of data acquisition for each instrument. As is shown in the figure, two of the instruments, ISAMS and CLAES, are no longer operating. ISAMS ceased taking data after a chopper wheel failed in mid-January 1992. The instrument was restarted 2 months later, but the mechanism failed permanently in July 1992. In April 1993 the CLAES cryogen expired on schedule, and the instrument ceased taking data. At about the same time, the MLS 183-GHz radiometer, which measured stratospheric water vapor and mesospheric ozone, failed. The other radiometers and constituent measurements made by the MLS were unaffected by this failure.

Starting in May 1995, persistent problems with the solar arrays and batteries necessitated the implementation of a power-sharing plan for the remaining functioning instruments. As is shown in Figure 1, most instruments presently take measurements for a few days during each yaw cycle. UARS has operated successfully

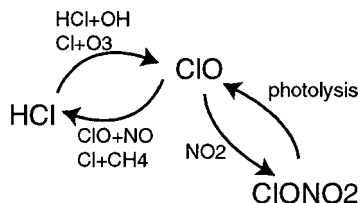


Figure 2. Schematic of interconversion pathways among inorganic chlorine molecules. Each arrow is labeled with the reactant that facilitates the conversion.

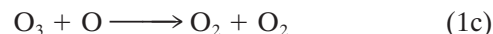
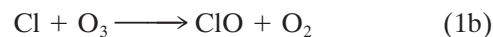
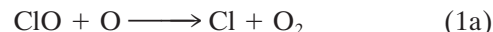
in this power-sharing mode for over a year and is expected to continue collecting data for several more years.

Finally, the conversion of measurements of radiance, the quantity that the satellite instruments actually measure, to physical parameters such as constituent mixing ratio occurs through “retrieval algorithms.” Over the 5 years of the UARS mission, many improvements to these algorithms have occurred, and periodically the radiances are reprocessed and improved sets of physical parameters are produced. To keep track of these changes, each set of physical parameters is assigned a version number. Higher version numbers refer to the parameters produced from more recent algorithms. In general, but not always, the highest available version of data is the most scientifically useful.

3. CHLORINE PARTITIONING

Most of the chlorine found in the stratosphere entered this region as a component of a man-made chlorofluorocarbon (CFC) molecule [Russell *et al.*, 1996b]. Once in the stratosphere, CFCs are broken up by ultraviolet photons, releasing the chlorine atoms. The chlorine atoms then undergo chemical reactions that convert them into other species. Virtually all of the chlorine in the stratosphere that is not in the form of a CFC is bound up in three molecules: HCl, ClONO₂, and ClO. During the day in the lower and mid stratosphere, the species HCl and ClONO₂ contain about 90% of this non-CFC chlorine, with ClO composing a major fraction of the remainder. At night, ClO reacts with NO₂ to form ClONO₂, and the sum of HCl and ClONO₂ then contains >97% of the total. For convenience, we define a new constituent known as “total inorganic chlorine” or Cl_y to be the sum of the concentrations of HCl, ClONO₂, ClO, and several other minor constituents. In other words, the concentration of Cl_y represents the concentration of non-CFC chlorine atoms, regardless of their particular molecular form.

How stratospheric chlorine is partitioned among these molecules turns out to be an important issue. As was pointed out by Stolarski and Cicerone [1974], the ClO radical catalyzes the destruction of ozone (O₃) by participating in catalytic loss cycles such as



The rate at which a catalytic cycle destroys ozone is determined by the slower of the two steps, which is known as the rate-limiting step. For almost all of the chlorine catalytic cycles, the rate-limiting step is a reaction in which one of the reactants is the ClO radical (e.g., for the ClO-Cl cycle shown above, the rate-limiting step is reaction (1a)). It is also well known that the rate of a reaction is proportional to the product of the concentrations of the reactants, in the case of (1a), ClO and O. Thus a knowledge of the concentration of ClO is required to quantitatively determine the ozone loss rate from the chlorine catalytic cycles. This, however, requires a knowledge of how Cl_y is partitioned among its primary members HCl, ClONO₂, and ClO.

Despite the importance of chlorine chemistry for regulating the abundance of stratospheric ozone, prior to the UARS program our theories of the partitioning of stratospheric chlorine had not been rigorously tested, primarily due to a lack of measurements. The UARS data set, however, is the first that contains measurements of all three of the important Cl_y members: HCl, ClONO₂, and ClO. In addition, instruments on UARS measure other species, in particular NO₂ and O₃, that affect the partitioning of the Cl_y species. The UARS data set thus allows a rigorous test of the partitioning of Cl_y between these three species (see Dessler *et al.* [1995, 1996b] for a review of the previous literature on Cl_y partitioning).

Chlorine catalysis is an important regulator of ozone throughout the stratosphere. In this section, however, we will emphasize the region of the stratosphere between 20- and 30-km altitude. Most of the Earth’s ozone lies in this region, and obtaining an understanding of the impact of humankind on the loss rate of ozone in this region is one of the most important challenges of stratospheric science and a primary goal of the UARS mission. We will demonstrate in this section that these UARS data suggest that our understanding of chlorine chemistry is generally good over this altitude range.

A schematic of chlorine partitioning is shown in Figure 2. During the day, ClONO₂ is photolyzed by visible and ultraviolet photons to produce Cl atoms [DeMore *et al.*, 1994], which react with O₃ essentially instantaneously to produce ClO. ClO reacts with NO₂ to reform ClONO₂. The timescale for chlorine to cycle through these species is an hour to several hours in the lower and mid stratosphere.

While the majority of ClO reacts to form ClONO₂, a small fraction of the ClO undergoes a two-step process that converts it to HCl: ClO reacts with NO to form Cl atoms, and then the Cl atoms react with CH₄ or H₂ to form HCl. HCl is lost through reaction with OH to form

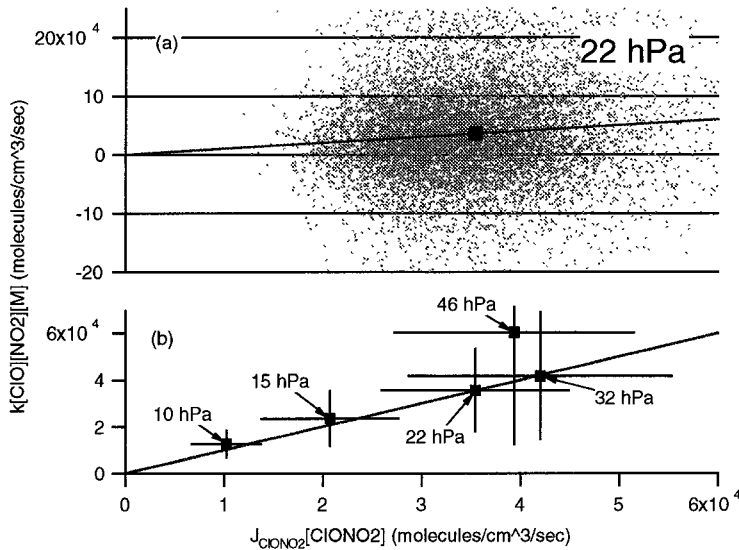


Figure 3. (a) Instantaneous production of ClONO₂ ($k[\text{ClO}][\text{NO}_2][\text{M}]$) versus loss of ClONO₂ ($J_{\text{ClONO}_2}[\text{ClONO}_2]$) on the 22-hPa pressure surface. Each dot represents a simultaneous measurement of ClO, NO₂, and ClONO₂ and a calculation of J_{ClONO_2} and k . The square is the average production and loss rate. The line is the one-to-one line. (b) Average production and loss rates on the 10-, 15-, 22-, 32-, and 46-hPa surfaces. Error bars represent accuracy estimates; precision uncertainty is negligible and is not considered. Note the agreement between average production and loss. The data were obtained between January 1 and April 15, 1993, and between 20° and 60° latitude in both hemispheres. Adapted from Dessler *et al.* [1996b].

Cl atoms, which subsequently reform ClO through reaction with O₃. The timescale for chlorine to cycle through HCl is a week to several tens of days in the lower and mid stratosphere.

Because the time required for interconversion between ClO and ClONO₂ is orders of magnitude shorter than the time for interconversion between ClO and HCl, we can divide the problem of Cl_y partitioning into two separate parts: the partitioning between ClO and ClONO₂ and the partitioning between HCl and the sum of ClO and ClONO₂.

3.1. ClONO₂-ClO Partitioning

Over most of the day, we expect that the formation of ClONO₂ through reaction of ClO with NO₂ is balanced by the loss of ClONO₂ through photolysis. This condition of balance, known as steady state, can be written as

$$k_{\text{ClO}+\text{NO}_2}[\text{ClO}][\text{NO}_2] = J_{\text{ClONO}_2}[\text{ClONO}_2] \quad (2)$$

where $k_{\text{ClO}+\text{NO}_2}$ is the effective two-body rate constant (cm³ molecule⁻¹ s⁻¹) for the reaction between ClO and NO₂ to form ClONO₂, J_{ClONO_2} is the photolysis rate constant (s⁻¹) for the photolysis of ClONO₂, and $[x]$ is the number density (molecules cm⁻³) of constituent x . Despite the fundamental importance of the balance in equation (2), until UARS was placed in orbit, stratospheric measurements to test the validity of (2) were not available.

To test equation (2), we use UARS measurements of ClO from the MLS [Waters *et al.*, 1996] (version 3), NO₂ (version 7) from the CLAES that has been adjusted by comparison with HALOE NO and NO₂ measurements [Dessler *et al.*, 1996b], and CLAES measurements of ClONO₂ [Mergenthaler *et al.*, 1996] and temperature [Gille *et al.*, 1996] (both version 7). The details of the J_{ClONO_2} calculation are given by Dessler *et al.* [1996b].

Figure 3 plots the formation rate of ClONO₂ (left-hand side of (2)) versus the loss rate of ClONO₂ (right-

hand side of (2)) for conditions where steady state is expected to apply (solar zenith angles less than 80°). Figure 3a shows this comparison using data obtained at 22-hPa pressure. There are ~10,000 points in this plot; each one represents a simultaneous measurement of ClO, NO₂, and ClONO₂ and a calculation of the J_{ClONO_2} and $k_{\text{ClO}+\text{NO}_2}$. The data show considerable scatter, forming a cloud around the one-to-one line. The origin of the scatter (including negative values) in Figure 3a is likely due to the large precision uncertainty of the ClO measurements, the statistics of which have been discussed by Schoeberl *et al.* [1993] and Waters *et al.* [1996].

To eliminate the precision uncertainty, we average the instantaneous production and loss rates and plot average production and loss rate in Figure 3a as the square. Note that the square falls close to the one-to-one line, indicating that average production and loss of ClONO₂ balance, as expected from equation (2). Figure 3b shows a close-up of the averaged value for this surface, as well as the 10-, 15-, 32-, and 46-hPa pressure surfaces. This figure shows good agreement between averaged instantaneous production and loss of ClONO₂. Also shown are the accuracy error bars obtained from propagation of the uncertainties [Dessler *et al.*, 1996b, Table 1]. Despite the large spread in the raw data, we have averaged enough data that the precision uncertainty of the average is only a few percent, insignificant compared to the accuracy uncertainty.

In general, the agreement in Figure 3b is quite good. At 32 and 22 hPa, production and loss agree to within 1%. At 15 and 10 hPa, production exceeds loss by 13% and 23%, respectively. Part of the discrepancy at 15 and 10 hPa results from our neglect of additional loss pathways for ClONO₂ at high altitudes through reactions with O, Cl, and OH, which are expected to contribute 7–10% to the loss of ClONO₂. Overall, the agreement between production and loss at 32, 22, 15, and 10 hPa is good. At 46 hPa, production exceeds loss by about 50%.

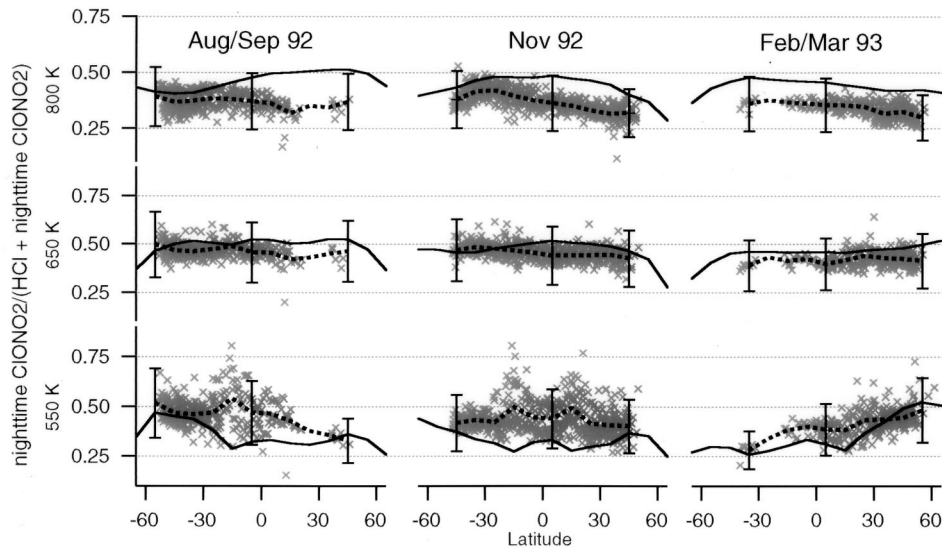


Figure 4. Plot of $[\text{nighttime ClONO}_2]/([\text{HCl}] + [\text{nighttime ClONO}_2])$ versus latitude. Both the individual UARS measurements (crosses) and an average of the UARS measurements (dashed lines) are shown. Error bars are estimates of the accuracy of the UARS ratio ($\pm 34\%$). The solid lines are calculations from the Goddard 2-D model. The top row is the 800-K potential temperature surface, the middle row is the 650-K surface, and the bottom row is the 550-K surface. The left column data are from August and September 1992, the middle column data are from November 1992, the right column data are from February and March 1993. Adapted from Dessler *et al.* [1995].

While within uncertainty limits, this agreement is much poorer than that at higher altitudes. More analysis of the 46-hPa data is necessary to determine the source of this disagreement.

Our analysis supports the simple balance expressed in equation (2): during the day, production and loss of ClONO_2 are equal. The UARS data offer the first opportunity to directly verify this crucial relation. We see no evidence to support missing chemistry, significant error in the rate constant for the reaction of ClO and NO_2 , or errors in our calculation of the photolysis rate of ClONO_2 .

3.2. HCl- ClONO_2 Partitioning

As was mentioned earlier, ClO is converted to HCl on a timescale that is orders of magnitude slower than that for conversion of ClO to ClONO_2 . In other words, on a timescale of the lifetime of HCl (weeks to months), ClO is rapidly interconverting with ClONO_2 . However, the sum of ClO and ClONO_2 has a lifetime that is similar to that of HCl, making this sum a convenient quantity to compare against HCl.

UARS measurements allow us to compare HCl and the sum of ClO and ClONO_2 . HCl is measured by the HALOE [Russell *et al.*, 1996a] (version 17), and ClONO_2 is measured by the CLAES [Mergenthaler *et al.*, 1996] (version 7). Because ClO is completely converted to ClONO_2 at night, we will use ClONO_2 measured at night to represent the sum of ClO and ClONO_2 . The primary difficulty with comparing HALOE HCl and CLAES ClONO_2 data is that the instruments do not make col-

located measurements. In order to compare these measurements made at different locations and times, we use the trajectory-mapping technique [Morris *et al.*, 1995]. Briefly, the method uses stratospheric wind data to determine where the air masses in which UARS measured HCl and nighttime ClONO_2 were on days before and after the measurement was made. If the air mass trajectory of a ClONO_2 measurement passed near a HCl measurement and the air was dynamically similar (as determined by potential vorticity), then these measurements are considered correlated. See Dessler *et al.* [1995] for more details of the calculation.

In Figure 4 we plot the quantity $[\text{nighttime ClONO}_2]/([\text{HCl}] + [\text{nighttime ClONO}_2])$, approximately the fraction of Cl_y that is in the form of nighttime ClONO_2 . The data are shown for three potential temperature surfaces: 550, 650, and 800 K, corresponding approximately to 21-, 24-, and 30-km altitude. These data suggest that Cl_y is fairly evenly distributed between ClONO_2 and HCl, with HCl the slightly more dominant reservoir over the range of potential temperatures, latitudes, and time considered in this paper.

The solid lines in Figure 4 are $[\text{nighttime ClONO}_2]/([\text{HCl}] + [\text{nighttime ClONO}_2])$ taken from a two-dimensional (2-D) model. See the discussion by Dessler *et al.* [1995] for a description of the model run. Over virtually the entire range of altitude and time covered in this analysis, the partitioning of Cl_y in the 2-D model (solid line) and in the UARS measurements (dotted line) agree within the accuracy error bars of the measurements. At 550 K (21 km), however, the model tends to

systematically overpredict HCl (and underpredict nighttime ClONO₂). The discrepancy has the same sign but has a smaller magnitude than that seen in the measurements made from the NASA ER-2 high-altitude aircraft [Salawitch *et al.*, 1994]. On the 650-K surface (24 km) the agreement between measured and predicted Cl_y partitioning is excellent. On the 800-K surface (30 km) the model tends to systematically underpredict HCl (and overpredict nighttime ClONO₂), a discrepancy that is opposite in sign to the disagreement on the 550-K surface. A similar difference at 800 K has been previously identified in measurements made by the shuttle-borne Atmospheric Trace Molecule Spectroscopy (ATMOS) instrument [e.g., Natarajan and Callis, 1991].

In conclusion, the UARS has provided an important new view into the partitioning of total inorganic chlorine into HCl and ClONO₂. In general, the data and a 2-D simulation agree within the uncertainties of the data. However, the comparison does reveal some discrepancies. Most notably, there appears to be an altitude-dependent systematic difference between the measurements and the model.

The combination of the ClONO₂-ClO and HCl-ClONO₂ analyses have provided the first complete view of chlorine partitioning in the stratosphere between 20 and 30 km. The general agreement between data and theory suggests that our theories incorporate the major mechanisms that interconvert the primary inorganic chlorine molecules: HCl, ClONO₂, and ClO. Some discrepancies remain, but they are generally within the uncertainties of the measurements.

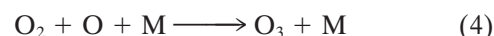
4. THE UPPER STRATOSPHERIC "OZONE DEFICIT"

Model simulations during the early to mid 1980s persistently predicted 40% to 60% less ozone than was measured in the upper stratosphere (~40- to 50-km altitude) [e.g., Crutzen and Schmailzl, 1983; Froidevaux *et al.*, 1985; Jackman *et al.*, 1986]. This discrepancy was important because these same models indicated that the primary stratospheric effect of chlorofluorocarbons (CFCs) would be a decrease in ozone around 40-km altitude [World Meteorological Organization (WMO), 1981, chapter 3]. Thus an understanding of this region was thought to be crucial for successfully identifying the first signs of man-made global change. This disagreement between models and measured O₃, which suggested problems with our understanding of upper stratospheric ozone chemistry, became known as the model "ozone deficit."

Over the next 10 years, our knowledge of the kinetic parameters and composition of the upper stratosphere improved greatly. The most recent models prior to the UARS [e.g., Siskind *et al.*, 1995; Eluszkiewicz and Allen, 1993; Minschwaner *et al.*, 1993], however, still predicted upper stratospheric ozone 10–25% less than measurements. (See Eluszkiewicz and Allen [1993] and Siskind *et*

al. [1995] for an overview of ozone budget studies.) As we will show in this section, data from the UARS have been used to perform the most detailed calculations of the ozone deficit. These analyses have suggested that the ozone deficit might be smaller than was expected and have confirmed a potential problem in which models overpredict ClO abundance in the upper stratosphere.

While models have improved in the last decade, the persistent ozone deficit is surprising because of the simplicity of ozone chemistry in this region of the stratosphere. Because of the short lifetime of upper stratospheric ozone, transport of O₃ can be neglected, and the assumption can be made that production of ozone and loss of ozone are balanced when averaged over 24 hours. Ozone is produced by the reactions



where M is an O₂ or N₂ molecule and $h\nu$ represents an ultraviolet photon. Ozone in the upper stratosphere is destroyed predominantly by reaction cycles in which a catalyst X is involved (X = NO, Cl, H, or OH):



as well as the direct reaction between O₃ and O to form two O₂ molecules.

The search for the cause of the disagreement between models and measurements of upper stratospheric ozone led to speculation about additional ozone production mechanisms besides reactions (3) and (4) [Slanger *et al.*, 1988; Miller *et al.*, 1994]. However, additional calculations have not supported the atmospheric significance of any such mechanisms [e.g., Latimer *et al.*, 1996; Toumi, 1992].

With the launch of the UARS, a new set of chemical trace gas measurements in the upper stratosphere became available. Many of the measurements are relevant to upper stratospheric ozone chemistry and have significantly improved our knowledge on this subject. For example, HALOE and MLS provide measurements of the two primary components of chlorine in the upper stratosphere: HCl and ClO. NO₂, the radical involved in the rate-limiting step of the nitrogen catalytic cycle, is measured throughout the day by CLAES and at sunrise and sunset by HALOE. Finally, a knowledge of O₃ is essential for testing our knowledge of the chemistry of the upper stratosphere. Four instruments on board UARS measure O₃, allowing validation of this important measurement.

These UARS data have been used to address this model ozone deficit. Crutzen *et al.* [1995] used simultaneous measurements of O₃, H₂O, HCl, CH₄, NO, and NO₂ from the HALOE instrument (version 17) to inves-

tigate the ozone budget. This marked the first time that direct measurements of chlorine species had been incorporated into a calculation of upper stratospheric O_3 . The calculations employed a newly developed iteration technique using the Mainz photochemical box model to derive the diurnal dependence of all important chemical trace gases, including species not measured by HALOE. The integration of chemical species over 1 day was repeated until the iteration converged to a diurnal cycle of chemical species consistent with the HALOE sunrise or sunset observations.

Figure 5 shows the ozone production rate P , the total ozone destruction rate D , and the ozone destruction rate attributed to the individual catalytic cycles as determined by the Crutzen et al. model, all averaged over 24 hours. Above 35 km the production rate and the total destruction rate show reasonable agreement, as expected by theory. In the upper stratosphere above ~ 45 km, the ozone destruction catalyzed by HO_x ($H + OH + HO_2$), or D_H , is the dominant process, whereas between ~ 25 - and 40-km altitude, destruction catalyzed by NO_x ($NO + NO_2$), D_N , is most important. The chlorine-catalyzed ozone destruction cycle D_{Cl} peaks at about 40-km altitude with a 30% contribution to the total ozone loss. Direct ozone loss via the reaction $O_3 + O \rightarrow 2O_2$, D_O , is most important at near 47-km altitude.

The net ozone production over 24 hours is also calculated by the model. Positive net ozone production indicates that the model predicts higher ozone than is measured (a surplus), while negative net ozone production indicates that the model predicts lower ozone than is measured (a deficit). Figure 6 shows the 24-hour net ozone production (as a fraction of measured ozone). The calculations were performed for single days using zonal averages of the HALOE data (from 15 events per day near the same latitude). Near 40-km altitude, all calculations show a balanced ozone budget within $\pm 1\%$.

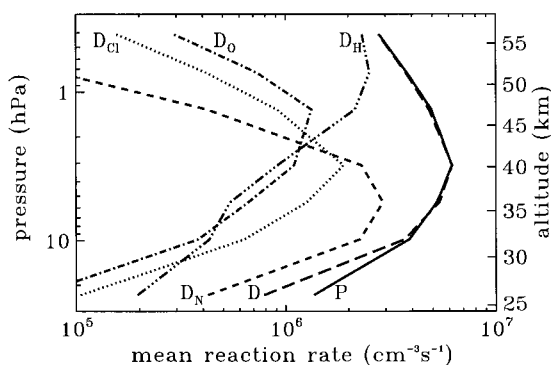


Figure 5. The calculated 24-hour average total ozone destruction rate D and the production rate P as a function of altitude (pressure). Also shown are the contributions from the individual chemical families (D_O , D_N , D_H , and D_{Cl}) to the total destruction rate D . Reprinted with permission from Crutzen et al. [1995]; copyright 1995 American Association for the Advancement of Science.

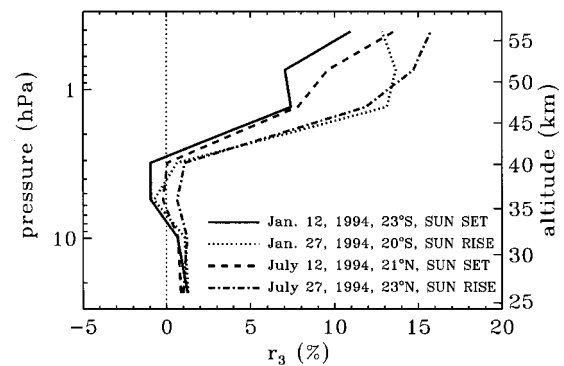


Figure 6. The calculated ozone increase over a 24-hour period during the last day of integration relative to the observation by HALOE, as a function of altitude (pressure) for different measurements at subsolar points in both hemispheres and both sunrise and sunset data as indicated in the legend. Compared to r_3 [Crutzen et al., 1995], the reaction rates [DeMore et al., 1994] and the $O(^1D)$ quantum yield [Michelsen et al., 1994] were updated. Reprinted with permission from Crutzen et al. [1995]; copyright 1995 American Association for the Advancement of Science.

A small model ozone surplus of 10–15% above 45-km altitude is calculated. This should be contrasted with recent calculations that predict model ozone deficits of 10–25% in this region [Siskind et al., 1995; Eluszkiewicz and Allen, 1993; Minschwaner et al., 1993].

It must be recognized, however, that these deviations from balance are smaller than the calculation's uncertainty, which include systematic errors in the HALOE data and uncertainties in rate coefficients. The validation of the HALOE data by correlative measurements shows that the mixing ratios in the version 17 data tend to have a low bias [Harries et al., 1996; Brühl et al., 1996; Gordley et al., 1996; Russell et al., 1996a]. At 40-km altitude a model ozone deficit of 9% was found when the O_3 , H_2O , HCl , and NO_x HALOE data used in the calculation were all increased by their estimated maximum possible bias. The use of the current HALOE retrieval (version 18) instead of version 17 in these calculations leads to a decrease of the 24-hour net ozone production by about 8% above 40-km altitude, resulting in a deficit of 5–10% at 40 km and an improved balance above. Inclusion of an HCl product channel in reactions of ClO with OH and HO_2 [Finkbeiner et al., 1995; Lipson et al., 1997] would increase the 24-hour net ozone production. These issues will be addressed in a forthcoming publication. Crutzen et al. [1995] showed that a change in the rate coefficients of the key HO_x reactions ($OH + O \rightarrow H + O_2$, $HO_2 + O \rightarrow OH + O_2$, and $HO_2 + OH \rightarrow H_2O + O_2$) by the maximum possible amount within the uncertainty range changed the ozone loss by at most $\pm 7\%$ at 40 km and $\pm 17\%$ at 52 km. Thus the difference between production and loss can be entirely explained by uncertainties in the parameters going into the calculation.

Dessler et al. [1996a] also examined the error budget

of the ozone production and loss calculation. Taking the uncertainties of all of the parameters entering into the calculation into account (rate constants, J values, and constituents), they estimated the total uncertainty (1σ) of the ozone deficit calculation to be $\pm 30\%$ (in this case, $15 \pm 30\% = -15\%$ to 45%). Importantly, they also pointed out that the selection of parameters going into the model had a large effect on the answer. Just by changing the ozone data set used in the calculation (e.g., HALOE versus MLS) and by varying the latitude of the calculation, a range of answers between a model deficit of 15% and a model surplus of 20% was obtained. Taking such a large uncertainty into account, there is no disagreement between the *Crutzen et al.* [1995] and *Dessler et al.* [1996a] deficit calculations, or between these analyses and other recent ozone deficit calculations [*Siskind et al.*, 1995; *Minschwaner et al.*, 1993; *Eluszkiewicz and Allen*, 1993].

The UARS data also provide evidence to support a suspected problem with the standard photochemistry of the upper stratosphere. Prior to UARS, there was indirect evidence that models did not accurately predict ClO in the upper stratosphere [e.g., *Minschwaner et al.*, 1993]. This has important ramifications because of the significant role ClO plays in regulating the abundance of ozone, especially near 40 km. The UARS data provide direct measurements that suggest that this problem does indeed exist. ClO measured by the UARS MLS is about 50% less than that predicted by a model utilizing a standard photochemical reaction set (with no production of HCl from the reaction between ClO and OH) [*Dessler et al.*, 1996a]. As can be seen from Figure 5, chlorine catalysis is responsible for significant ozone destruction between 40 and 46 km, and this overestimate of ClO by standard models could result in an overestimate of total ozone loss by 10–40%. It should be noted that not all models of the upper stratosphere reproduce this discrepancy; more research on this topic is necessary.

In conclusion, the analysis of UARS data has provided additional insight into the model “ozone deficit” in the upper stratosphere. Recent ozone budget calculations of *Crutzen et al.* [1995] and *Dessler et al.* [1996a] based on UARS data show ozone production and loss balancing to within 20%, in rough agreement with the pre-UARS analyses. These UARS analyses reveal a balanced ozone budget within their given uncertainty limits, even though they used different approaches.

5. OBSERVATIONS OF THE MOUNT PINATUBO AEROSOL CLOUD AND POLAR STRATOSPHERIC CLOUDS

The importance of heterogeneous chemistry, i.e., reactions of gas species with liquid and solid particles, in the stratosphere was dramatically demonstrated when it became clear that the formation of the Antarctic ozone hole was predicated on the occurrence of heterogeneous

processes. The general conditions under which the Antarctic ozone hole develops are now well defined (see *WMO* [1992, chapter 3] for a review of the causes of the Antarctic ozone hole). First, temperatures in the lower stratosphere must be low enough that polar stratospheric clouds form from the condensation of water vapor and HNO_3 . Reactions on the surfaces of PSCs combined with sunlight convert chlorine from inactive reservoir species (HCl , ClONO_2) to the ozone-destroying radical ClO. Under sufficiently cold conditions ($T < \sim 189$ K), the PSCs can grow large enough to precipitate, leading to permanent removal of HNO_3 from the lower stratosphere. Our present understanding of ozone hole formation suggests that the precipitation of HNO_3 -rich aerosols is a crucial step because if they are not removed, the reaction set



would lead to the conversion of ClO back into the reservoir species ClONO_2 in a few days. The formation of the Antarctic ozone hole, however, requires elevated ClO for several weeks. Second, PSC-processed air must be exposed to sunlight to drive the catalytic cycles that destroy ozone. Third, PSC-processed air must be isolated so that mixing of processed air with midlatitude air does not inhibit the perturbed chemistry that is responsible for the ozone hole.

The importance of heterogeneous chemistry was further emphasized when it was realized that reactions on sulfuric acid aerosol particles also have an effect on the chemistry of the stratosphere [*WMO*, 1995]. Mainly, the reaction of N_2O_5 on the surfaces of these droplets forms HNO_3 . Because HNO_3 has a longer lifetime than N_2O_5 , the net result of this reaction is that NO and NO_2 are reduced in comparison with aerosol-free conditions. The reduction in NO_2 in turn causes the balance between ClONO_2 and ClO to shift in favor of ClO [*Fahey et al.*, 1993; *Dessler et al.*, 1993]. These reactions are critical for obtaining a quantitatively accurate picture of the stratosphere.

UARS instruments have observed sulfuric acid aerosol particles at equatorial and middle latitudes and PSCs within the southern and northern polar regions. Aerosol extinction measurements have been made by several UARS experiments, and volcanic SO_2 gas has been measured by the MLS experiment. Uncertainties associated with the aerosol data are discussed by *Lambert et al.* [1996a], *Massie et al.* [1996a], and *Hervig et al.* [1996]. In this section we discuss the picture that the UARS has provided of the evolution of the aerosol cloud that resulted from the June 1991 eruption of Mount Pinatubo, as well as the location, timing, and chemical effects of polar stratospheric clouds.

Mount Pinatubo erupted 3 months before the launch of UARS, and injected nearly 20 Mt (2×10^{10} kg) of

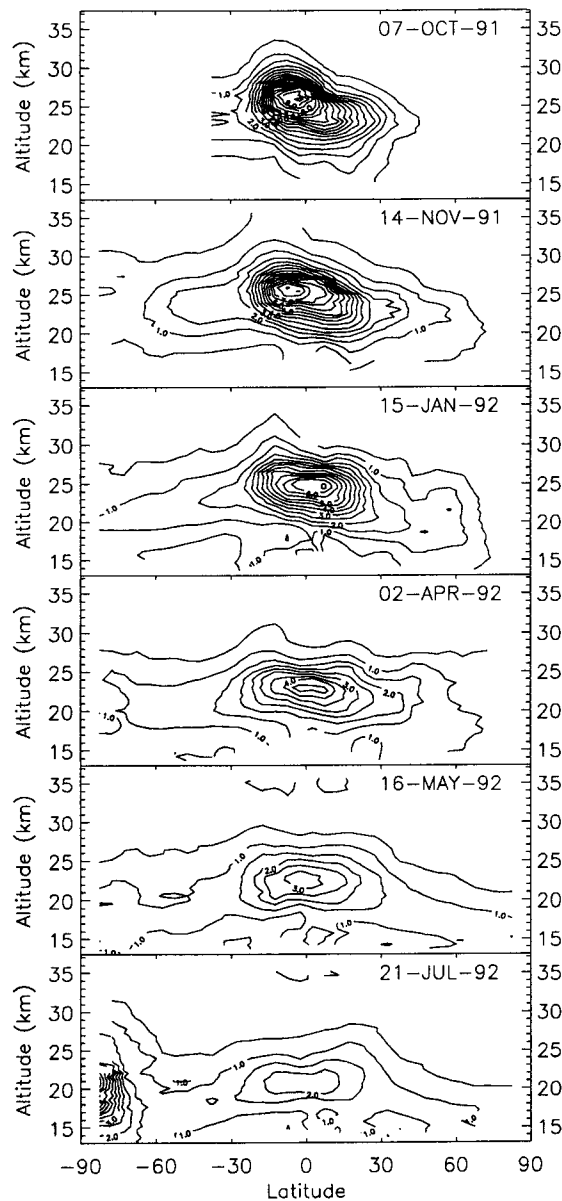


Figure 7. Zonal mean of the 12.1- μm extinction (in units of $10^7 \text{ m}^2 \text{ mol}^{-1}$) observed by ISAMS in the period October 1991 to July 1992. A zonal mean is constructed by averaging all measurements from a specified latitude and altitude, but covering all longitudes. The extinction coefficient is the effective cross section (in square meters) per mole of air, with higher values indicating a greater ability to reduce the intensity of a beam of light. From Lambert *et al.* [1993, Figure 2].

SO_2 gas into the stratosphere [McCormick and Veiga, 1992; Mergenthaler *et al.*, 1995]. The Mount Pinatubo eruption was one of the largest of the century and perturbed stratospheric temperature, chemistry, and optical depths in both the visible and infrared [WMO, 1995; Granier and Brasseur, 1992; Young *et al.*, 1994; Coffey, 1996; Kinnison *et al.*, 1994]. The timing of the launch of UARS allowed its observations of temperature and constituents to be used to study the effects of heterogeneous chemistry upon the stratosphere.

Volcanic SO_2 gas was measured by the MLS beginning on the first day of observations on September 19, 1991 [Read *et al.*, 1993]. As displayed in Figures 2–4 of Read *et al.* [1993], SO_2 mixing ratios peaked in the latter part of September near 15 ppbv at 26-km altitude and decayed thereafter with an e -folding time of ~ 33 days. The decay of SO_2 is due to the reaction



where M is an O_2 or N_2 molecule. The MLS data are consistent with column amounts of SO_2 observed by the Total Ozone Mapping Spectrometer (TOMS) and Solar Backscattered Ultraviolet (SBUV) satellite experiments and by aircraft instruments, which reported measurements 0 to 30 days past the June 1991 eruption.

The HSO_3 formed in reaction (9) is subsequently oxidized to form H_2SO_4 , which then reacts with water vapor to form sulfuric acid droplets. Transport and vertical sedimentation spread the volcanic aerosol cloud poleward and downward. Figure 7 displays ISAMS 12.1- μm extinction for the period October 1991 to July 1992. On October 7, 1991, the bulk of the aerosol cloud is distributed asymmetrically about the equator, with highest concentrations near 26-km altitude. High aerosol extinction is evident all the way to the south pole on November 14, 1991. By January 15, 1992, the region of highest extinction is over the equator at 24 km. The double-peaked structure, seen between 20°S and 20°N beginning in January 1992, is a consequence of the mean meridional stratospheric circulation [Trepte and Hitchman, 1992]. During the descending westerly phase of the quasi-biennial oscillation (QBO), which was established in the January–July 1992 time frame, there is downward transport over the equator. Peak equatorial aerosol extinction also descended with time owing to sedimentation. From Figure 3 of Lambert *et al.* [1993], the observed change in the altitude of the peak aerosol extinction is consistent with particle radii of 0.2–0.3 μm . As the aerosol is transported toward the polar regions, it may enhance the formation of PSC particles [Hofmann and Oltmans, 1993]. In Figure 7, PSCs are present in the data for July 21, 1992, poleward of 70°S.

Confirmation that the observed extinction at equatorial and mid-latitudes is due to $\text{H}_2\text{SO}_4/\text{H}_2\text{O}$ droplets is obtained from the wavelength dependence of the aerosol extinction. The wavelength dependence of the aerosol extinction is due to both composition (which determines the index of refraction) and particle size. Comparisons of observed UARS data with model calculations show that the extinction data are consistent with the presence of sulfuric acid droplets [Grainger *et al.*, 1993; Massie *et al.*, 1994, 1996b]. These results are also consistent with spectra measured by the shuttle-borne Atmospheric Trace Molecule Spectroscopy (ATMOS) instrument [Rinsland *et al.*, 1994].

It is expected that aerosol extinction data from sulfate droplets from the eruption of Mount Pinatubo and PSCs

should have different characteristics due to different particle sizes and composition. To quantify these differences, *Massie et al.* [1994] introduced the “aerosol spectral measure” (M) value. The aerosol measure is calculated by forming a triangle with x coordinates calculated using the observation wavelengths at 6.23, 7.95, and 10.8 μm and the y coordinates calculated using the aerosol extinction values at these wavelengths. The shape of the triangle changes as particle size and composition (indices of refraction) change. Using this triangle and an algebraic formula, an M value is extracted. For sulfuric acid aerosol at equatorial and middle latitudes, values of M range between -2 and -1 , while for PSC particles (at cold temperatures within the polar regions), M is typically greater than 0. *Massie et al.* [1994, Figure 13] graph aerosol extinction versus temperature for observations on August 18, 1992, in the southern polar regions at 6.23, 7.95, and 10.8 μm . The figure displays large extinction at temperatures less than 195 K, due to the presence of PSCs. The dependence of M versus temperature, using these data [*Massie et al.*, 1994, Figure 14], displays M values that are positive at the coldest temperatures, also indicative of the presence of PSCs.

Aerosol extinction cannot be used directly to calculate rates of reaction of heterogeneous reactions. Calculations of heterogeneous reaction rates instead require surface area and volume densities, in other words, the surface area and volume of the aerosol present per unit volume [*Hanson et al.*, 1994]. As developed by *Grainger et al.* [1995] for ISAMS data and used by *Massie et al.* [1996b] for CLAES data, reasonable estimates of the area and volume densities can be calculated from UARS extinction data. The ratio of particle radius to wavelength is small for stratospheric particles at infrared wavelengths, and the extinction is therefore proportional to the volume density. The relationship between volume and surface area density can be determined by an empirical power law scaling and modeled using observed size distributions such as the sulfate aerosol size distribution measurements of *Deshler et al.* [1993].

Geller et al. [1995] and *Yudin et al.* [1997] investigated the atmospheric effects of PSC reactions using a three-dimensional chemistry-transport model of the distribution of chlorine species in the northern hemisphere polar region. These papers use a simplified parameterization of PSC processing and reproduce the observed relationships between fields of temperature, potential vorticity (which marks the boundary of the dynamical structure known as the “polar vortex”), aerosol extinction and aerosol measure, HCl, ClONO₂, and ClO. Their analysis shows that the coldest temperatures within the polar region are associated with large aerosol extinction values and positive aerosol measure M values, suggesting that PSCs exist in these regions. At warmer temperatures, the aerosol measure is in the range -2 to -1 , characteristic of sulfuric acid droplets. In addition, the sum of HCl and ClONO₂ is ~ 2 ppbv outside the polar vortex, while inside the polar vortex the sum is



Plate 1. Plot of 465-K (~ 50 hPa) vortex conditions for December 1 through March 20, 1991–1992 through 1995–1996: (a) minimum National Centers for Environmental Prediction (NCEP) temperatures in the Arctic vortex region (defined by the 1.2 contour of scaled potential vorticity [e.g., *Manney et al.*, 1994] calculated from NCEP winds and temperatures). The thin horizontal line at 195 K represents the approximate PSC formation threshold, and the line at 188 K represents the approximate temperature at which PSCs sediment. The dark shaded region shows the range of minimum NCEP Arctic vortex temperatures between 1978–1979 and 1990–1991, and the light shaded region shows the range of minimum temperatures for the Antarctic between 1992 and 1996 (Antarctic values begin in June, the equivalent season to December in the Arctic). (b) Vortex-averaged MLS ClO. (c) Vortex-averaged MLS ozone. The large gaps in MLS data in January are when MLS was observing the southern hemisphere. MLS data were not obtained every day during the 1994–1995 and 1995–1996 winters; the symbols show all of the days for which complete MLS data are available. Adapted from *Manney et al.* [1996a, b] and *Santee et al.* [1996].

~ 0.9 ppbv. Daytime MLS ClO mixing ratios show enhanced values of ClO inside the vortex. *Geller et al.* [1995] conclude that air that has been processed through regions of cold temperature (in which PSCs have formed) have chemical characteristics that are consistent with the chemical effects of PSC processing.

In conclusion, UARS data present an opportunity to

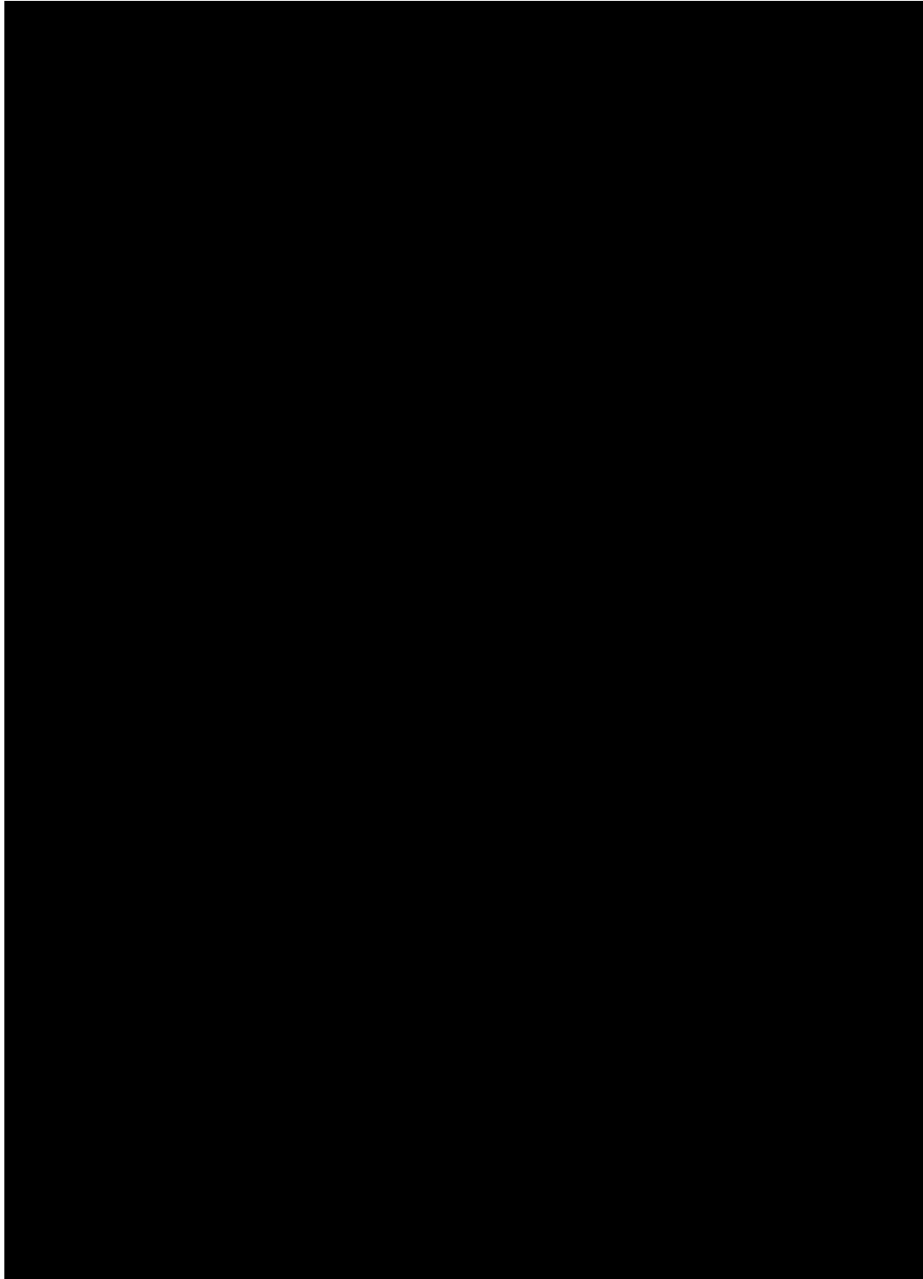


Plate 2. Latitude-height cross sections of CF_2Cl_2 mixing ratio as observed by CLAES during (top) March and (bottom) September 1992 [Nightingale *et al.*, 1996]. There is a mean decrease with height due to photolytic destruction. Mixing ratio isopleths are displaced upward in the tropics and downward in the extratropics by the global-scale circulation. The effects of mixing in the extratropical surf zones are shown by weak meridional gradients in middle latitudes bounded by strong gradients in the subtropics, and in the September section at the edge of the winter polar vortex.

study the effects of heterogeneous chemistry on the stratosphere. The development of the Antarctic “ozone hole” and of seasonal ozone loss episodes over the Arctic is dependent upon the presence of PSCs. In addition, reactions on sulfuric acid aerosol particles at all latitudes have a major impact on the chemical system that regulates stratospheric ozone. Instruments on board the UARS measure many of the variables in the lower stratosphere that are important for quantitatively testing our understanding of heterogeneous reactions: temper-

ature; gas phase mixing ratios of ClONO_2 , HCl , and HNO_3 ; and the PSC-aerosol extinction (from which area and volume densities are derived).

6. LOSS OF OZONE IN THE ARCTIC LOWER STRATOSPHERE

As was discussed in section 5, the causes of the Antarctic ozone hole are well defined. Interestingly,

many of these conditions also occur in the Arctic. First, in virtually every year, the temperatures are low enough (~ 196 K) for PSC processing [Zurek *et al.*, 1996; Manney *et al.*, 1996a] (Plate 1a), leading to the formation of enhanced abundances of the ozone-destroying ClO radical (Plate 1b). Second, the polar region is exposed to sunlight, driving the catalytic cycles that destroy ozone. Third, the polar region is isolated, although less so than in the Antarctic [e.g., Manney *et al.*, 1994], and this isolation allows the ClO catalytic cycles to destroy ozone. Despite these similarities, an Arctic “ozone hole” has yet to form.

Our present understanding suggests two reasons for the lack of an Arctic ozone hole. First, while air parcels in the Arctic are exposed to temperatures cold enough to form PSCs, the temperatures are not generally cold enough that the particles grow large enough to precipitate out of the stratosphere. Plate 1a shows that while the temperatures do get below 195 K, the PSC formation threshold, they only rarely drop below 189 K, thought to be the threshold temperature for growth of the particles to sizes required for precipitation. Thus when the Arctic air parcels warm up, the particles evaporate, and HNO_3 is released back into the stratosphere. Reactions (7) and (8) subsequently convert the ClO back into ClONO_2 . Because of this, average ClO abundance during the period of maximum ozone loss in the Antarctic (late winter through early spring, mid-August through mid-October) is much greater than that during the comparable period in the Arctic.

Second, the time that the Arctic polar region (often referred to as the polar vortex) remains isolated from the midlatitudes is a shorter duration than in the southern hemisphere. This is important because when the polar vortex breaks up, PSC-processed air mixes with unprocessed midlatitude air, severely inhibiting the loss of ozone due to ozone hole chemistry. Because of this, the dissipation of the polar vortex marks the end of ozone destruction by polar chemistry. Therefore the ozone loss processes operate over a shorter time period in the Arctic than the Antarctic, and therefore by the end of the ozone loss period, these loss processes have destroyed less ozone.

While an ozone hole does not form in the northern hemisphere, there is evidence that ozone hole chemistry is destroying significant amounts of ozone in the northern hemisphere [WMO, 1995]. Among the most important research performed with the UARS data is quantification of the loss of ozone at high latitudes in the northern hemisphere. The UARS observations provide a set of simultaneous and collocated measurements with daily hemispheric coverage of many species, facilitating analysis of processes taking place throughout the polar vortex. These measurements include the first measurements with hemispheric coverage of several important species (e.g., ClO, ClONO_2). In this section we will summarize several UARS analyses of Arctic ozone loss and show that while an Arctic ozone hole has not

formed, substantial chemical loss of ozone is occurring. These analyses have dramatically improved our understanding of polar processes.

The primary obstacle to quantifying the loss of ozone in the Arctic is quantifying the effects of transport on the ozone distribution. Transport effects typically increase ozone in the polar lower stratosphere over the course of a winter because the descent of air in the winter polar regions, due to the mean meridional circulation (see section 7), transports air with high mixing ratios of ozone into the lower stratosphere from above. Horizontal transport from midlatitudes, on the other hand, occasionally decreases ozone by transporting midlatitude air (with lower ozone) into the vortex. In other words, even when chemical loss is occurring, the ozone mixing ratio at a given point can still increase in time if the transport of ozone-rich air from above is larger than the chemical loss. Alternatively, a decrease in ozone could occur even in the absence of chemical loss if ozone-poor midlatitude air is transported into the polar vortex [Schoeberl *et al.*, 1990]. Therefore a quantitative evaluation of ozone transport is necessary before a quantitative evaluation of chemical loss of Arctic ozone is possible. It should also be noted that these transport effects are less important in the Antarctic. The polar vortex there is strong and stable, and the vertical transport of ozone-rich air and horizontal transport of ozone-poor air into the lower stratosphere are negligible in comparison with ozone loss in this region. This means that in the Antarctic, changes in lower stratospheric ozone are almost solely due to chemical loss [Manney *et al.*, 1995a].

Plate 1c shows vortex-averaged 465-K (~ 20 km) ozone mixing ratios observed by MLS. Many of the changes are suggestive of chemical loss. Day-to-day variability and uncertainties in the data, however, are sufficiently large that it is difficult to definitively attribute this small change to chemical loss. In order to separate the effects of transport from chemistry, calculations using a diabatic reverse trajectory procedure [Manney *et al.*, 1995a, b, c, 1996a, b] have been performed. Briefly, an initial measured ozone distribution is advected forward in time by analyzed or assimilated wind fields using trajectory calculations [Sutton *et al.*, 1994] just as a passive tracer would be. Comparisons between the ozone predicted by the passive tracer calculations and subsequent measurements of ozone allow a quantitative evaluation of chemical ozone loss. UARS passive tracer observations validate these transport calculations [Manney *et al.*, 1995c]. Figure 8 shows both measured ozone and vortex-averaged ozone computed using only transport at 465-K potential temperature (~ 20 km). The difference between these values is caused by chemical loss. In 1994 (Figure 8a), descent of ozone-rich air cancels most of the chemical ozone loss. The net result is that vortex-averaged ozone remains fairly constant despite estimated chemical loss of nearly 0.5 ppmv of ozone. In contrast, in 1996 (Figure 8b) there was less transport of ozone-rich air from above, and significantly

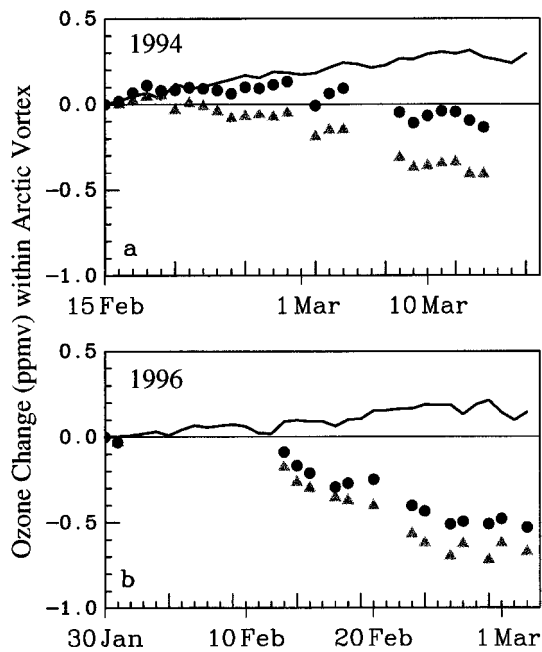


Figure 8. Vortex-averaged chemical ozone change (triangles) estimated as the difference between the observed ozone (black dots) and the ozone calculated using transport alone (line), for 30-day periods in February and March of the (a) 1993–1994 and (b) 1995–1996 Arctic winters. Observations and calculations performed at 465 K (~ 20 km). Adapted from Manney *et al.* [1995b, 1996a].

greater chemical loss. Chemical loss and transport of ozone in other winters fall between these two extreme cases. The largest ozone decrease rates observed in the Arctic are typically one-half to two-thirds those in the Antarctic at the equivalent time of year, and chemical ozone destruction stops much earlier in the season in the Arctic. As was mentioned previously, because Antarctic loss is larger and replenishment by descent is smaller, transport masks very little of the ozone loss seen there [Manney *et al.*, 1995a]. Müller *et al.* [1996] compared HALOE CH_4 and ozone relationships for the Arctic vortex in early and late winter during the winters of 1991–1992, 1992–1993, 1993–1994, and 1994–1995. Their results, which are broadly consistent with those from the MLS, show evidence of chemical ozone loss in each year.

Analysis of UARS observations has thus demonstrated that chemical loss is occurring in the polar lower stratosphere. It is more difficult to discern the effect of this loss on the total ozone in the column. The layer over which ozone mixing ratios decrease in the lower stratosphere typically contributes $\sim 1/3$ of the column [e.g., Froidevaux *et al.*, 1994]; a 30–50% decrease in lower stratospheric ozone would thus produce a 10–15% decrease in column ozone in the absence of other effects. Dynamically induced variations greater than this are common. It is therefore difficult to unambiguously attribute changes in the column to chemical loss. In the

Antarctic, on the other hand, balloon-borne ozonesonde measurements show a 100% decrease over a larger region of the lower stratosphere and about a 60–70% decrease in column ozone (much larger than dynamical variability) during the late winter and early spring [e.g., Hofmann *et al.*, 1994].

Analysis of UARS observations of ozone, passive tracers, and several species involved in chemical ozone destruction has resulted in an improved understanding of Arctic ozone loss. UARS observations show evidence of ozone loss in the Arctic vortex during each of the past 5 Arctic winters due to ozone hole chemistry. There is substantial interannual variability both in the amount of chemical ozone loss and in the transport processes that are the other important factor in producing observed ozone changes. Ozone increases due to transport tend to mask a substantial portion of chemical ozone loss in the Arctic, so that while Arctic ozone depletion has thus far always been considerably less than that in the Antarctic, it is frequently significantly more than would be suggested by the ozone observations alone.

7. STRATOSPHERIC TRANSPORT DEDUCED FROM UARS MEASUREMENTS

The spatial and temporal distributions of trace constituents in the stratosphere are in general dependent on both chemistry and transport. Long-lived constituents are those constituents for which the chemical timescale (defined as the characteristic time for replacement or removal due to sources and sinks) is longer than the dynamical timescale (defined as the characteristic time for advective and diffusive processes to transport the tracer from equator to pole or vertically through a scale height). Of special interest for transport studies are constituents such as nitrous oxide, methane, and the CFCs, which have long tropospheric lifetimes but are destroyed through photolysis or oxidation in the stratosphere at rates which increase with height. The mixing ratios of such constituents in a given air parcel are dependent on the total exposure of the air in that parcel to photochemical destruction and hence provide information on the global-scale circulation [McIntyre and Palmer, 1984]. In this section we will show how the wide range of measurements made by the UARS has verified our theories of both short- and long-timescale transport in the stratosphere.

The time mean global-scale circulation consists of strong east-west (i.e., zonal) winds, which tend to homogenize trace constituents in the longitudinal direction, and an overturning circulation in the meridional (latitude-height) plane involving cross-isentropic upwelling in the tropics and downwelling in the extratropics (an isentropic surface is one of constant entropy and is approximately horizontal). In addition, there are longitudinally asymmetric waves that tend to disperse trace constituents north-south (i.e., meridionally) on isen-

tropic surfaces. Long-lived tracers are thus subject to cross-isentropic advection and along-isentropic dispersion. Figure 9 shows a schematic of the zonal mean circulation of the stratosphere. Cross-isentropic advection and along-isentropic dispersion are not, however, independent processes. Both are now known to be associated with wave breaking in the extratropical stratosphere. Wave breaking is responsible for a wave-induced force that nonlocally controls the global-scale cross-isentropic circulation. Wave breaking also produces rapid dispersion of tracers along the isentropes [Holton *et al.*, 1995; McIntyre, 1992; Plumb and Ko, 1992].

This transport paradigm is supported by long-lived tracer observations from the UARS. For example, Plate 2 shows a height versus latitude cross section of CF_2Cl_2 from CLAES. The overall distribution of the tracer is in agreement with the schematic circulation shown in Figure 9. Surfaces of constant mixing ratio are displaced upward in the tropics and slope downward toward the poles in the extratropics, consistent with advection by the cross-isentropic global-scale circulation. In midlatitudes there are regions in which tracer mixing ratio isopleths are nearly horizontal, reflecting the horizontal homogenizing role of meridional dispersion by planetary wave breaking. The same processes also tend to homogenize the potential vorticity (PV) distribution on isentropes in the middle latitudes. PV may be thought of as a fluid dynamical analog of spin angular momentum. It is normally positive in the northern hemisphere and negative in the southern hemisphere, consistent with the sense of the Earth's rotation, and increases in absolute value with latitude on isentropic surfaces. This middle latitude region, also known as the "surf zone," is bounded at both low and high latitudes by strong meridional gradients of long-lived tracers and of PV. The existence of such gradients is evidence that there is only weak mixing into and out of the tropics and into and out of the polar winter vortex. Thus these locations are sometimes referred to as "transport barriers." The strong PV gradients, strong winds, and strong wind shears that occur along the transport barriers at the subtropical and polar edges of the surf zone all act to suppress wave breaking and hence to minimize mixing and sustain the strong gradients at those locations. On the other hand, rapid meridional dispersion occurs in the surf zone of the winter hemisphere extratropics, where planetary wave activity is strong and PV gradients are weak.

As a result of weak mixing of air from higher latitudes into the tropics, air entering the stratosphere in the tropics retains for many months the composition that it had on entry into the stratosphere as it is slowly pulled upward in the tropics by the global-scale circulation. This so-called "tape recorder" effect [Mote *et al.*, 1996] is strikingly demonstrated by the time-height section of total hydrogen shown in Plate 3. Total hydrogen is here defined as the sum of 2 times the methane mixing ratio plus the water vapor mixing. Since each methane mole-

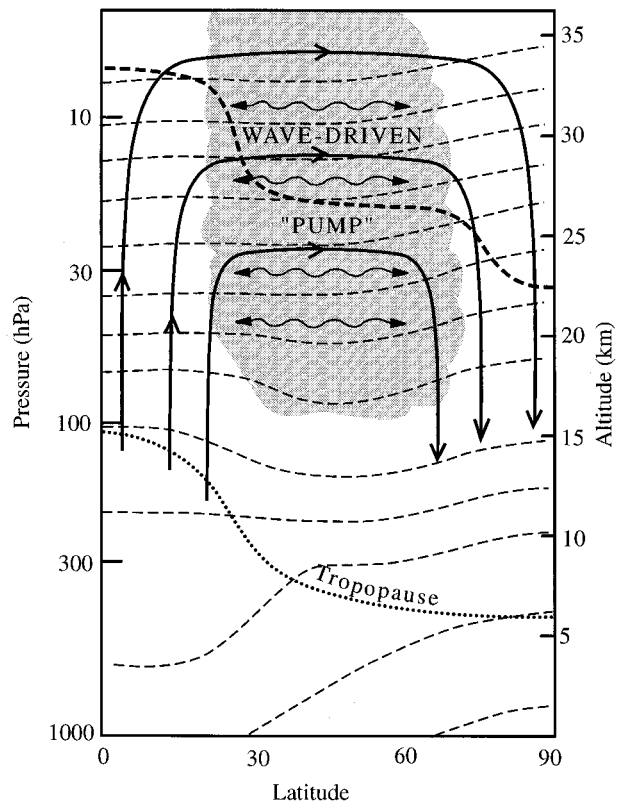


Figure 9. Schematic of stratospheric transport in the meridional plane. The tropopause is shown by the heavy dotted line. Thin dashed lines are isentropes. The heavy arrows show the global-scale circulation driven by the extratropical pump. The heavy dashed line shows a contour of constant mixing ratio for a long-lived trace constituent. For more details of the "wave-driven pump," see Holton *et al.* [1995].

cule is normally oxidized to produce two water molecules [e.g., Dessler *et al.*, 1994], total hydrogen should be approximately conserved in the stratosphere except in the polar winter vortices, where the sedimentation of large ice particles can cause dehydration. Furthermore, because methane is nearly constant at the tropical tropopause, variations in the mixing ratio of total hydrogen on entry to the stratosphere are determined by changes in the water vapor mixing ratio. These, in turn, are controlled by the tropopause temperature because air parcels usually enter the stratosphere with water vapor mixing ratios close to ice saturation mixing ratios, and saturation mixing ratios are strongly temperature dependent. The annual variation in the tropopause temperature is in turn determined by variations in the strength of the upwelling and its accompanying adiabatic cooling [Yulaeva *et al.*, 1994].

The tropical upwelling varies seasonally with a maximum at the solstice seasons. However, stronger wave generation in the northern hemisphere causes the upwelling to be greater in the northern hemisphere winter than in the southern hemisphere winter. Thus the coldest tropical tropopause, and lowest water vapor mixing ratio on entry into the stratosphere, occurs in northern

hemisphere winter. Hence the mixing ratio of total hydrogen at the tropopause varies annually with a minimum in northern winter and maximum in northern summer, and as is clear from Plate 3, the mixing ratio imprinted at the tropopause is pulled upward ~ 10 km over the course of a year with very little loss of amplitude.

Above ~ 25 km the annual signal does decay with height, indicating that some mixing must occur with extratropical air [Minschwaner et al., 1996; Avallone and Prather, 1996; Mote et al., 1996; Volk et al., 1996]. This mixing of air across the subtropical transport barrier occurs primarily when wave breaking associated with large-amplitude Rossby waves irreversibly pulls filaments of tropical air into the midlatitudes and filaments of midlatitude air into the tropics [Randel et al., 1993]. Similar processes of mixing caused by filamentation occur at the edge of the winter polar vortex.

The UARS has provided detailed information on the meridional dispersion of trace constituents by breaking waves. The most interesting studies of isentropic transport and mixing have combined UARS data with accurate isentropic parcel-following trajectory calculations. These calculations reveal that the stretching and folding of material contours by the large-scale wind field can rather quickly produce fine-scale filamentary structure that is irreversible. Such calculations have been carried out for a number of UARS-observed constituents. An example is shown in Plate 4, where the contour advection technique of Norton [1994] is employed to advect the abundance of sulfuric acid that is contained in aerosols. The figure shows results from a run using United Kingdom Meteorological Office (UKMO) assimilated winds initialized 6 days earlier with data derived from the ISAMS. Deep poleward intrusions of filaments of air with high sulfuric acid content and equatorward protrusions of air with low concentrations of sulfuric acid illustrate the sort of irreversible deformation of material contours and tracer dispersion that is associated with wave breaking.

In conclusion, the UARS data have helped refine our understanding of transport processes in the stratosphere. The data have confirmed our theories of the zonal mean transport being a combination of cross-isentropic (i.e., vertical) advection and along-isentropic (i.e., horizontal) dispersion. In doing so, these analyses have demonstrated the importance of transport barriers in the stratosphere. In addition, the UARS data, in concert with high-resolution trajectory studies, have illuminated the role of Rossby wave breaking in the meridional dispersion of trace constituents.

8. OBSERVATIONS OF MIDDLE AND UPPER ATMOSPHERIC WINDS

Direct measurements of wind are made by the UARS HRDI and WINDII instruments [Hays et al., 1989; Shep-

herd et al., 1993]. HRDI provides coverage in the stratosphere (10–50 km) and in the mesosphere and lower thermosphere (MLT) region (50–115 km), while WINDII makes measurements in the thermosphere (90–300 km). Line of sight wind measurements are taken on the atmospheric limb in two orthogonal directions, thus allowing the horizontal wind vector to be formed. The length, spatial coverage, and altitude range of the UARS wind data set has facilitated new investigations of the seasonal and interannual behavior of global dynamical fields in the stratosphere, mesosphere, and thermosphere.

8.1. MLT Tides and Mean Winds

To a first approximation the dynamics of the global MLT region can be characterized by a superposition of tidal waves on the prevailing wind field. Thus an accurate description of tides and mean winds is essential to a complete understanding of the upper atmosphere. UARS has provided the first opportunity to obtain global long-term observations of these fundamental phenomena.

Atmospheric tides are wave perturbations that are driven by the solar heating cycle. Studies of the tidal dynamics of the MLT region from UARS are complicated because on a given day the local time of the orbit is fixed at each latitude. A slow precession in the orbit provides 24-hour local time coverage over a period of about a month. Hays and Wu [1994] demonstrated that it is possible to estimate the contribution of the principal mode of the diurnal tide from a composite of one month's data and a single day's wind observations, resulting in daily values for the tidal amplitude [Hays and Wu, 1994]. This is because a large latitude coverage is typically available each day, and the data can be fitted to the well-known latitudinal structure of the dominant diurnal mode. WINDII uses an alternative approach to determine the amplitude and phase of the tides [McLan-dress et al., 1994], employing a simple Fourier decomposition of the local time variation provided by monthly data composites. These analyses allow the tidal components to be removed from the UARS data, permitting studies of the underlying field to be pursued.

The UARS tidal investigations include the first study from space of the migrating semidiurnal tide in the MLT region [Burrage et al., 1995a]. This provided a latitudinal and seasonal climatology of the phenomenon at an altitude of 95 km, which was chosen because it is only here that 24-hour local time coverage is available from HRDI [Burrage et al., 1994], permitting a simple Fourier decomposition to extract the semidiurnal tide. Because of the incomplete latitudinal coverage of ground-based techniques, the satellite study revealed new features of the tidal morphology. Regular seasonal changes and interhemispheric asymmetries were identified. Since WINDII is able to perform 24-hour local-time measurements over a range of altitudes (90–110 km), it has also been possible to extract information on the altitude

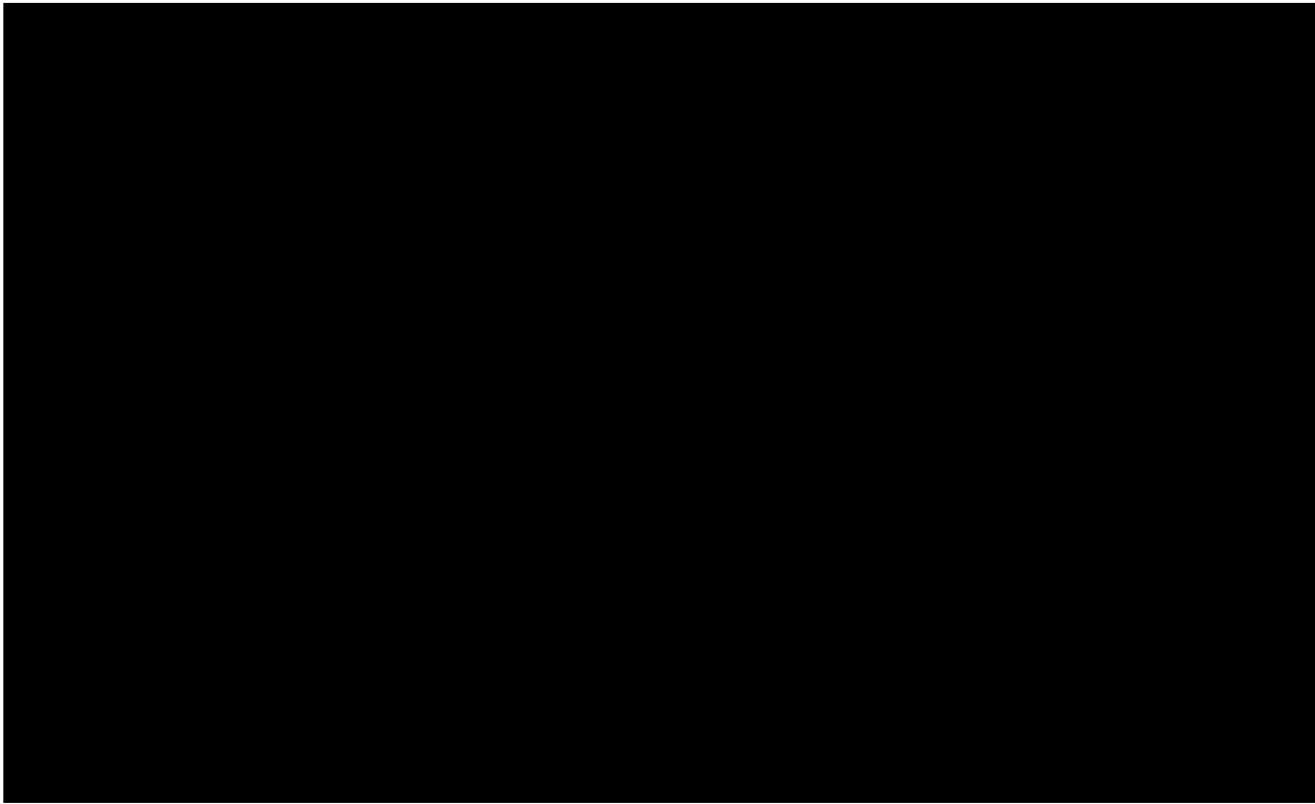


Plate 3. The atmospheric “tape recorder” [Mote *et al.*, 1996] is shown by a time-height cross section of total hydrogen ($2\text{CH}_4 + \text{H}_2\text{O}$) averaged between $\pm 8^\circ$ latitude from HALOE data. The annual cycle in total hydrogen at the tropopause is drawn into the lower and middle stratosphere by ascending air at a rate of $\sim 1 \text{ km month}^{-1}$ with little loss of amplitude below about 25 km. The cycle at the tropopause is phased so that low total hydrogen enters the stratosphere in northern winter while high total hydrogen enters in northern summer.

structure of the semidiurnal tide with UARS [McLandress *et al.*, 1996a].

At lower latitudes the wind fields are dominated by the diurnal tide [Hays *et al.*, 1992; Morton *et al.*, 1993; McLandress *et al.*, 1994]. The vertical wavelength of the dominant diurnal tidal mode is 23–25 km, and the amplitude grows with height up to an altitude of 100 km, above which it weakens owing to dissipation. At the equator the diurnal tide produces a dramatic perturbation in both the $\text{O}_2(^1\Sigma)$ [Burrage *et al.*, 1994] and the green line [Shepherd *et al.*, 1995] airglow emission rates because of changes in the distribution of atomic oxygen. Long-term observations of MLT winds obtained with HRDI have demonstrated that there is both a large semiannual variation [Hays and Wu, 1994] and a previously undetected interannual variation [Burrage *et al.*, 1995b] in the amplitude of the diurnal tide (Figure 10). The global-scale wave model (GSWM) [Hagan *et al.*, 1995] represents the first numerical modeling attempt to simulate the seasonal variability, and a preliminary comparison with the HRDI observations pointed to some critical and unresolved questions regarding tidal dissipation and tropospheric forcing [Burrage *et al.*, 1995b].

HRDI tidal determinations have been used to derive

estimates of tidal zonal and vertical winds, temperatures, and dissipation. Lieberman and Hays [1994] and Lieberman [1997] applied classical tidal theory to obtain estimates of the Eliassen-Palm flux divergence for the principal diurnal mode. The Eliassen-Palm flux is a measure of the momentum associated with the propagating tidal wave, and the divergence in this parameter indicates the degree of momentum transfer to the mean flow. The flux divergence is westward at all times in the equatorial lower thermosphere, with values ranging between -2 and $-16 \text{ m s}^{-1} \text{ d}^{-1}$ near 100 km. The tidal driving exhibits weak semiannual and interannual variations, with the largest values observed at equinox. The results suggest that the dissipating diurnal tide contributed to the maintenance of the time mean westward flow which is observed by HRDI in the equatorial lower thermosphere (90–105 km).

HRDI observations provide information about the long-term evolution of the zonal mean zonal wind throughout the middle atmosphere (10–115 km). By combining HRDI data with WINDII measurements, McLandress *et al.* [1996b] extended the coverage of the global background wind field up to an altitude of 200 km, revealing the two-cell structure of the thermospheric

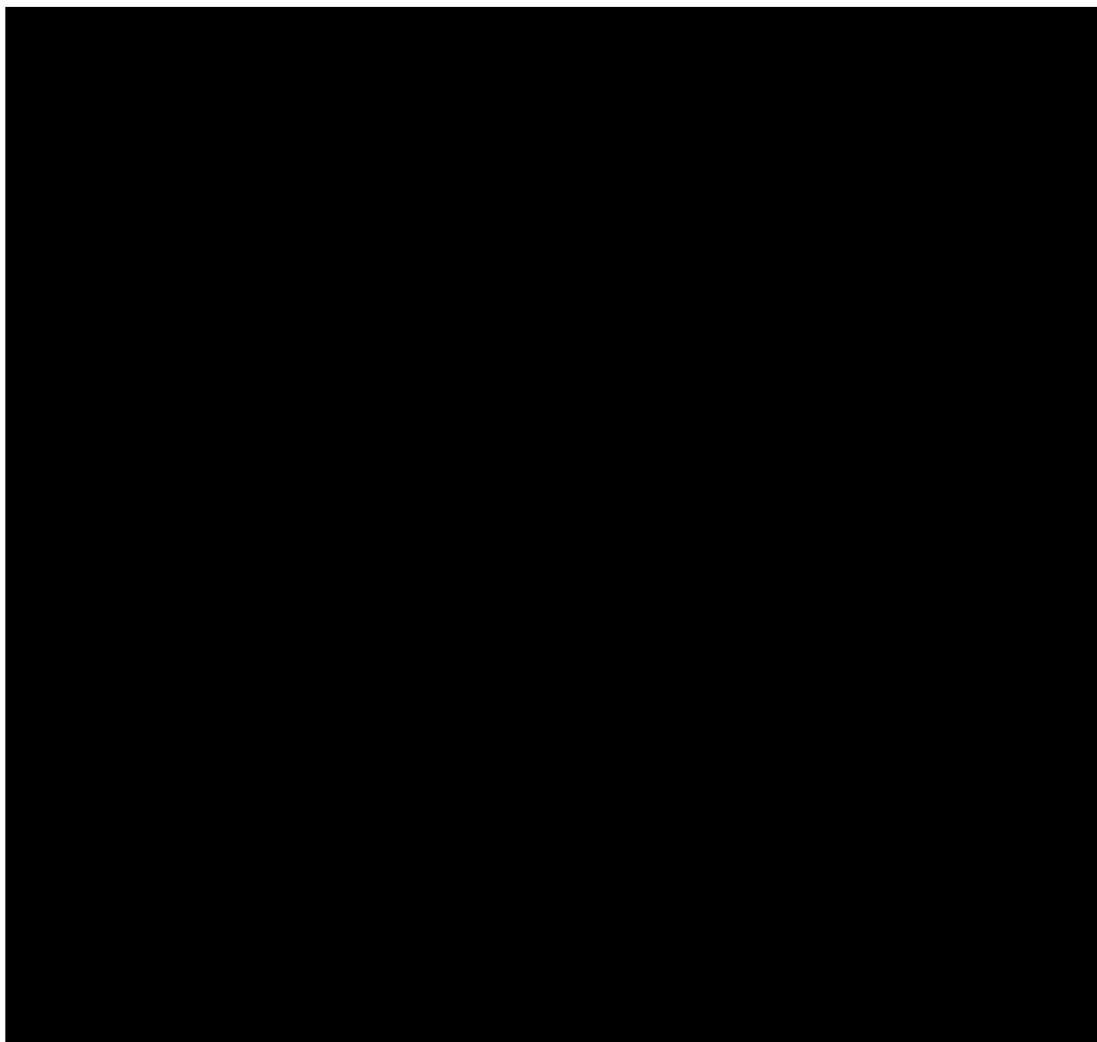


Plate 4. Northern hemisphere distribution of the sulfuric acid dissolved in aerosols for December 6, 1991 (day 340) on the 450-K isentropic surface as predicted by contour advection initialized 6 days previously with the ISAMS sulfuric acid data and using United Kingdom Meteorological Office (UKMO) assimilated winds. Darker colors indicate lower abundances of H₂SO₄. The Greenwich meridian is at the bottom, and the 0°, 30°N, and 60°N latitude circles are shown. Numbers show ISAMS measurement locations on December 6, 1991. Adapted from *Lambert et al.* [1996b, Figure 3e].

meridional circulation. The HRDI results are illustrated in Plate 5. The most prominent feature in the meso-

sphere is the mesosphere semiannual oscillation (MSAO) [*Lieberman et al.*, 1993].

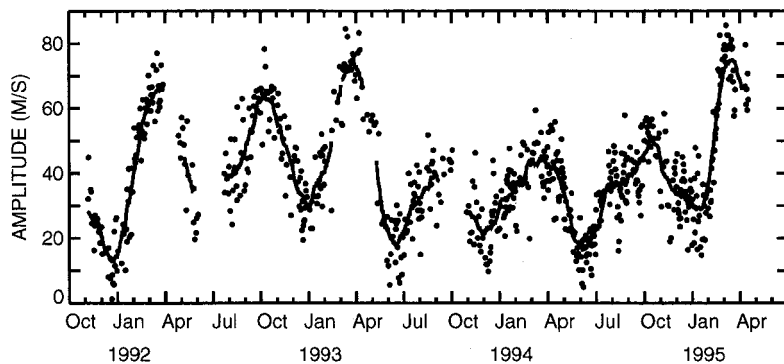


Figure 10. Daily amplitude estimates of the diurnal component of the meridional wind obtained from HRDI data for an altitude of 95 km and a latitude of 20°. The solid line is a 10-day running average, which serves to highlight the long-term variations.



Plate 5. Zonal mean wind observed by HRDI at the equator as a function of altitude (in kilometers) and time. The contour levels are given every 10 m s^{-1} . In the stratosphere the quasi-biennial oscillation (QBO) is clearly delineated, while in the mesosphere the most prominent feature is the mesosphere semiannual oscillation (MSAO). The mesosphere QBO is also very evident; note the anomalously large MSAO easterly phases occurring in March 1993 and March 1995.

The HRDI instrument has also revealed a 2-year variation in the mesospheric background zonal wind, which exhibits a clear relationship to the quasi-biennial oscillation in the stratosphere [Burrage *et al.*, 1996]. Preliminary model simulations [Mengel *et al.*, 1995] suggest that the observations may be explained in terms of the selective filtering of small-scale gravity waves by the underlying winds they traverse.

8.2. Stratospheric Winds and Waves

Accurate information on the dynamics of the stratosphere is critical to understanding how chemical trace species such as ozone are distributed through the atmosphere. In the past, the global wind field in the stratosphere was deduced indirectly from temperature measurements, and more recently from a combination of measurements and data assimilation techniques. The HRDI stratospheric wind measurements are an important new data set that provides coverage in the tropics, upper stratosphere, and southern hemisphere, all regions that are not well sampled by the global radiosonde network.

As was discussed in section 7, the dynamics of the

middle atmosphere is driven by the interplay of radiative heating and mechanical forcing by dissipating waves propagating up from the troposphere. This forcing generates a slow circulation in the meridional plane that redistributes angular momentum and chemical tracers. Observations of the waves present in the wind field and of the angular momentum distribution make it possible to quantify the magnitude of the forcing and deduce the structure of the circulation.

The annual cycle in solar heating drives a circulation in the stratosphere that transports air from the summer hemisphere to the winter hemisphere, resulting in summer easterly and winter westerly winds, by conservation of angular momentum. The westerlies, however, are not as strong as they would be if this were the only factor. Rossby waves propagate up from the troposphere and deposit easterly momentum into the stratosphere as they dissipate, slowing the westerlies. This wave forcing causes a circulation that brings air up from the tropics and down over the winter pole, producing higher tracer concentrations at a given altitude over the equator than at the same altitude at higher latitudes [Holton *et al.*, 1995] (see also section 7). There is more Rossby wave

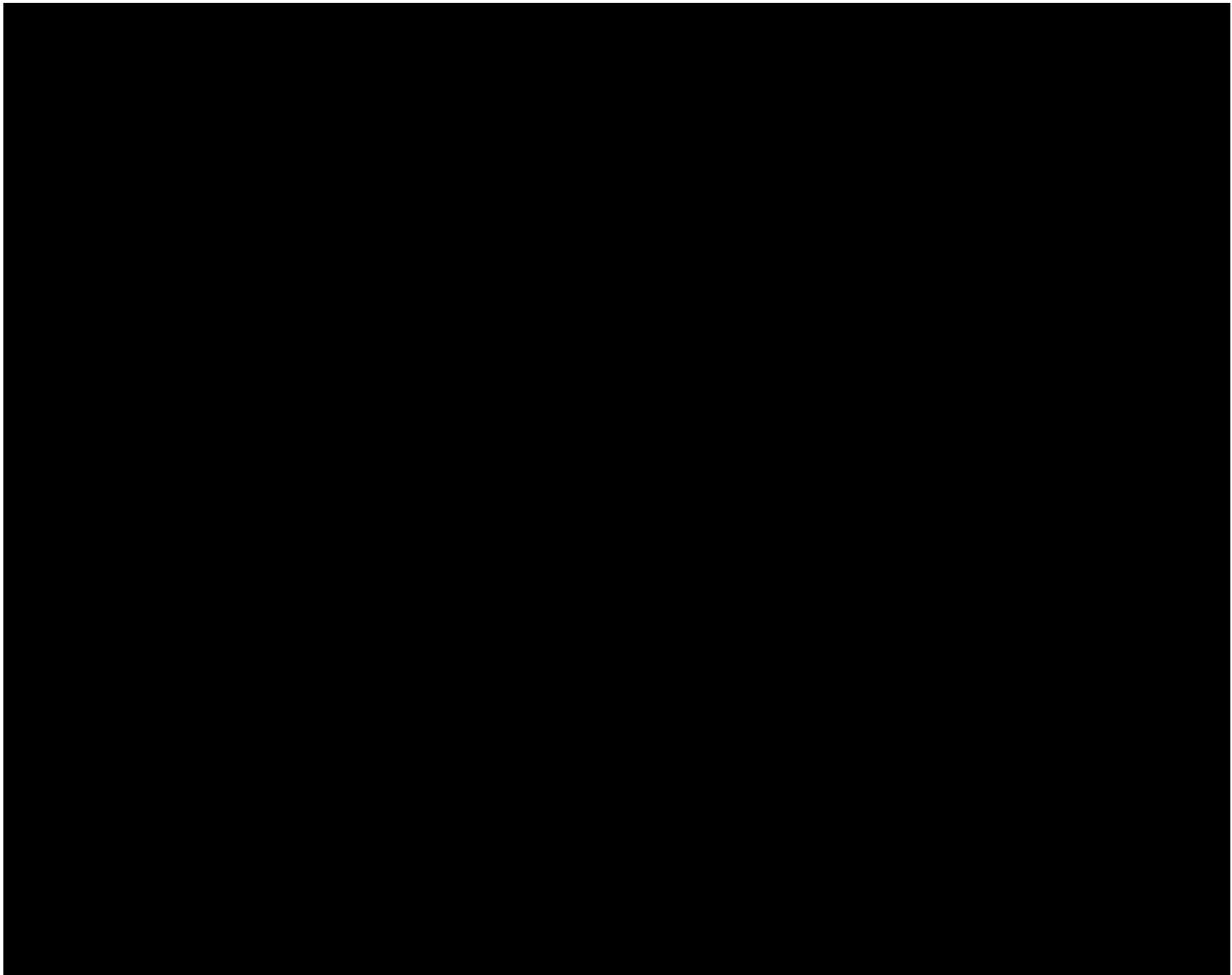


Plate 6. Time-latitude sections of monthly and zonally averaged zonal winds at (top) 25 and (bottom) 37.5 km. Contours are at 5 m s^{-1} intervals.

activity, generated by orography and land-sea temperature differences, in the northern hemisphere than in the southern, and thus the southern hemisphere westerlies are stronger.

A striking example of a wave-driven phenomenon in the equatorial stratosphere is the quasi-biennial oscillation. This can be seen in Plate 5 and in the top panel of Plate 6. Regions of mean easterly and westerly winds over the equator progress downward in an irregular cycle that repeats about every 27 months. The QBO is driven by the vertical transfer of momentum by waves generated in the tropical troposphere. In the two cycles of the QBO seen by HRDI so far, the westerlies above 30 km have a much shorter duration, and the phase lines descend much more rapidly than at lower altitudes. The transition from westerly to easterly winds above 30 km occurs during northern hemisphere winter in both QBO cycles observed by HRDI.

The strength of the semiannual oscillation (SAO) easterlies and westerlies are quite variable in the upper

stratosphere. Easterlies are generally stronger during northern winter, and this may be why the westerlies of the QBO above 30 km are cut short at this time. A pattern in the westerly strength is less clear. Note that SAO westerlies did not occur at 37.5 km in the northern spring of 1993 or 1995. This is also the time of the onset of QBO easterlies in the upper stratosphere and the anomalously strong easterlies of the mesosphere SAO as seen in Plate 5.

In conclusion, the HRDI and WINDII wind data sets have improved our understanding of the middle atmosphere dynamics. Studies of the stratosphere, mesosphere, and lower thermosphere have aided in the development of a more complete picture of the circulation of the middle and upper atmosphere. In particular, analyses of the mesosphere and lower thermosphere tides has illuminated this important component of the circulation of the upper atmosphere. Stratospheric wind measurements have also revealed some of the details of the QBO, a phenomenon of importance to the circulation of the stratosphere.

9. SOLAR IRRADIANCE VARIABILITY MEASURED BY UARS

The primary source of energy for the Earth's surface and atmosphere is the Sun. Changes in the amount of solar radiation reaching the Earth can therefore affect our environment, requiring a reliable specification of the Sun's radiative output variability in order to isolate anthropogenic global change from natural variability. Because the Sun's activity varies over multidecadal timescales and our climate is potentially sensitive to small changes in the solar output, precise long-term monitoring of solar radiative output is a component of NASA's Mission to Planet Earth [Asrar and Dokken, 1993; Hartmann et al., 1993]. Three of the ten instruments on UARS are presently monitoring solar radiative output with unsurpassed accuracy and precision. SOLSTICE [Rottman et al., 1993; Woods et al., 1993] and SUSIM [Brueckner et al., 1993] measure UV spectral irradiance from 120 to 420 nm, and ACRIM II measures total (spectrally integrated) irradiance [Willson, 1979, 1994].

Solar activity, the changing amount of magnetic flux in the Sun's atmosphere, continuously modulates the flux of radiation received by the Earth. So too does the Sun's rotation on its axis, which alters the distribution of magnetic active regions on the surface of the Sun projected at Earth. As a result, solar irradiance exhibits prominent quasi-cycles with periods near 11 years due to activity and 27 days due to rotation [Lean, 1991]. Space-based monitoring during the 17 years prior to the UARS detected an 11-year cycle in bolometric (spectrally integrated) radiation with an amplitude of about 0.1% [Willson and Hudson, 1991; Hoyt et al., 1992; Lee et al., 1995], and a superimposed rotational modulation of a few tenths percent. Space-based monitors also observed the Sun's UV radiation during this time, detecting rotational modulation of a few percent near 250 nm and as much as 40% in the HI Lyman alpha and shorter wavelength emission lines [Hinteregger et al., 1981; Heath and Schlesinger, 1986; Rottman, 1988]. However, these UV measurements lacked the long-term precision needed to characterize the amplitude of the 11-year cycle with sufficient certainty for global change studies. Indirect determinations based on extrapolations of empirical relationships, or scaling factors, of solar activity proxies with the more reliably measured rotational modulation suggested 11-year UV irradiance cycles of 8% near 200 nm and more than 50% at HI Lyman alpha [Cebula et al., 1992; Lean et al., 1992].

The UARS was launched near maximum levels of solar activity, as demonstrated by the 10.7-cm flux variations in Figure 11. UARS has subsequently tracked the Sun's irradiance throughout the declining phase of solar cycle 22 [London et al., 1993], a cycle surpassed in strength by only one other (cycle 19) since the anomalously low solar activity levels of the seventeenth-century Maunder minimum. Ground-based and other space-based solar observations gathered over the UARS time

period provide an array of complementary data with which to assess, interpret, and characterize the measured irradiance changes. In conjunction with atmospheric measurements made by other instruments on the UARS and simulations by atmospheric and climate models, UARS solar data are facilitating the exploration of solar-terrestrial connections over a variety of timescales [Balachandran and Rind, 1995; Chandra et al., 1995; Hansen et al., 1997].

Figure 12 shows the SOLSTICE and SUSIM 1-nm spectra during February 1992, for which solar activity levels were near the highest encountered by UARS. Differences between SOLSTICE and SUSIM 1-nm spectral irradiances are typically less than $\pm 10\%$. Exceptions are in the vicinity of pronounced spectral features and for the rapidly decreasing fluxes at wavelengths less than 140 nm, where the two spectra can differ by more than 30% because of small signals with uncertain contributions of scattered light and wavelength registration. Over broader (>3 nm) wavelength bands, the SOLSTICE and SUSIM spectral irradiances generally agree to within $\pm 5\%$ at wavelengths longer than 150 nm and have been validated by their comparable agreement with UV spectra measured by the shuttle-borne ATLAS payload [Woods et al., 1996]. SOLSTICE performs in-flight radiometric tracking using periodic comparisons of the Sun's signal with an average signal from multiple bright blue stars. SUSIM performs in-flight radiometric tracking using its on-board deuterium lamps and multiple redundant optical elements. The long-term precision goal of the SOLSTICE and SUSIM measurements is $\pm 1\%$. However, differences exist in the abilities of the SOLSTICE and SUSIM to track both short-term rotational modulation and long-term solar cycle trends. This is evident in Fig. 11, where from the beginning to the middle of 1992 the 200-nm irradiances diverge from each other by 3%. SOLSTICE's superior wavelength registration sustains short-term precisions that approach, at times, a few tenths of a percent, compared with 1% for SUSIM. The differences between the UV irradiances measured by SOLSTICE and SUSIM are, however, less than the uncertainties in solar irradiance variability deduced from the historical database and may change with subsequent versions of the data reduction algorithms.

ACRIM II measures the Sun's total radiative energy without wavelength discrimination by directly comparing incoming solar and electrically generated power with an absolute accuracy of a few tenths of a percent. Three self-calibrating, dual-cavity pyrheliometers operate on different duty cycles, experiencing different rates of in-flight sensitivity degradation. Comparisons of long-term trends recorded by the radiometers with different duty cycles permit quantitative assessment of instrumental sensitivity drifts. Removing these instrumental effects from the measured signals enables determination of the actual changes in solar radiation with a long-term precision approaching a few hundredths of a percent [Will-

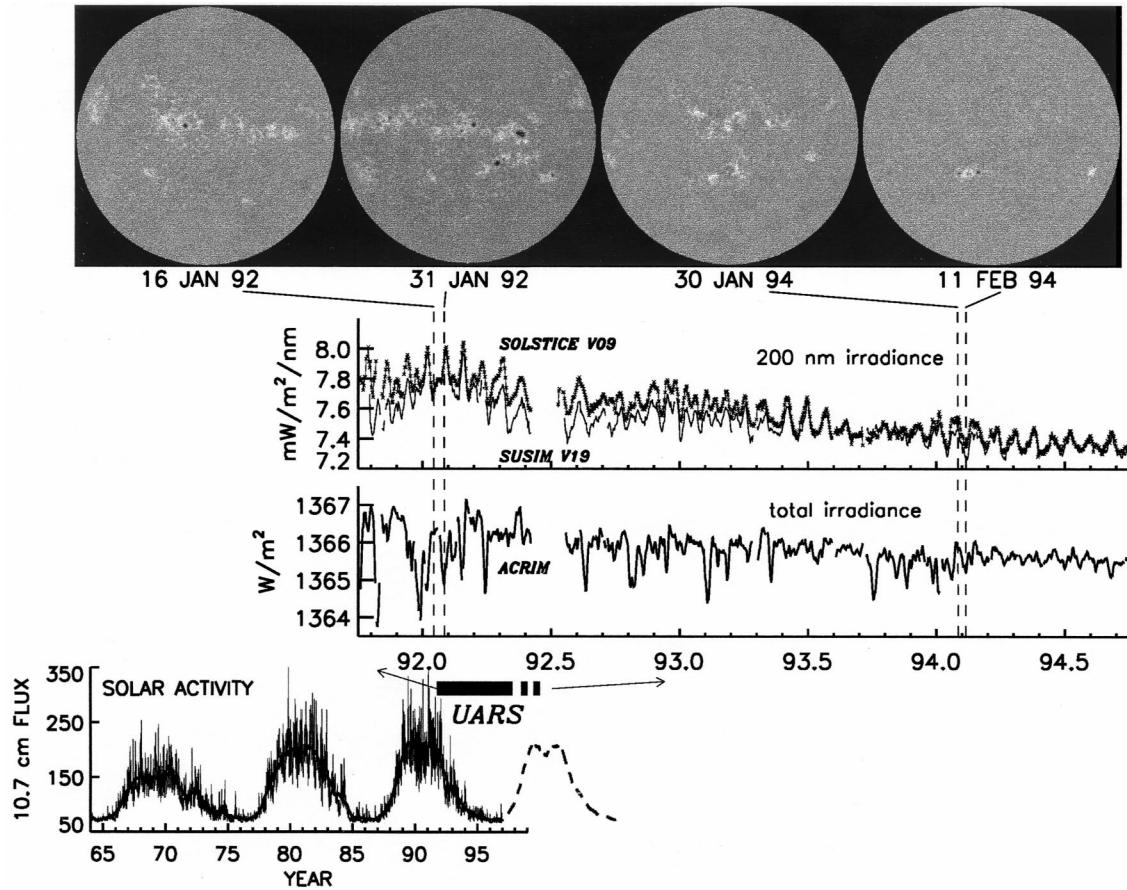


Figure 11. UARS solar monitoring has tracked the descending phase of solar cycle 22, which commenced in 1986, as indicated in the bottom panel by the 10.7-cm solar-activity record. Changing distributions of magnetic emission sources on the Sun's disk, shown in the four Ca K images, modulate both the UV radiation, shown in the top panel at 200 nm, and total irradiance, shown in the middle panel. As solar activity decreases, so too does the overall level of the Sun's radiative output in both total and UV wavelengths, as emissions from both dark sunspots and bright faculae decline.

son, 1979], which is adequate for the detection of the 11-year irradiance cycle. Sensitivity drifts typically occur during the initial measurements by space-based radiometers, and validation of ACRIM II observations is being accomplished by comparison with overlapping measurements made by Nimbus 7, the Earth Radiation Budget Satellite and the Solar and Heliospheric Observatory [Willson, 1994; Kyle et al., 1994; Mecherikunnel, 1994; Fröhlich, 1994].

The UARS solar monitoring extends the 17-year total irradiance record to the present, provides the first measurements of the spectral dependence of UV irradiances on solar activity made by instruments having end-to-end radiometric sensitivity tracking, and permits assessment of these UV energy changes to total irradiance variability over timescales of solar rotation and the 11-year solar cycle. Analysis of UARS solar measurements in conjunction with a variety of other solar data expands knowledge of solar variability beyond the measurement capabilities. The images of the Sun in Figure 11, made at the Big Bear Solar Observatory in the core of the Ca K Fraun-

hofer line [Johannesson et al., 1995], illustrate the connection between radiative output and the distribution of emission sources on the Sun's disk. During early 1992, near the maximum of solar cycle 22, magnetic active regions in the form of dark sunspots and bright regions, called faculae or plage, cover more of the Sun's disk than are covered during the lower activity levels of 1994. Increases in these features from January 16 to January 31, 1992, cause an increase in the 200-nm irradiance but a decrease in total irradiance. During lower solar activity and in the absence of major sunspots in January and February 1994, changing facular emission causes the UV and total irradiances to increase and decrease together.

Recognition of the competing influences of dark spots and bright faculae and plages, and their wavelength dependencies, provides a physical basis for parameterizing solar activity in order to reconstruct the Sun's radiative output in epochs beyond the UARS time frame, and in spectral regions where solar variability is smaller than UARS long-term monitoring capabilities. Figure 13 illustrates reconstructed solar irradiance time

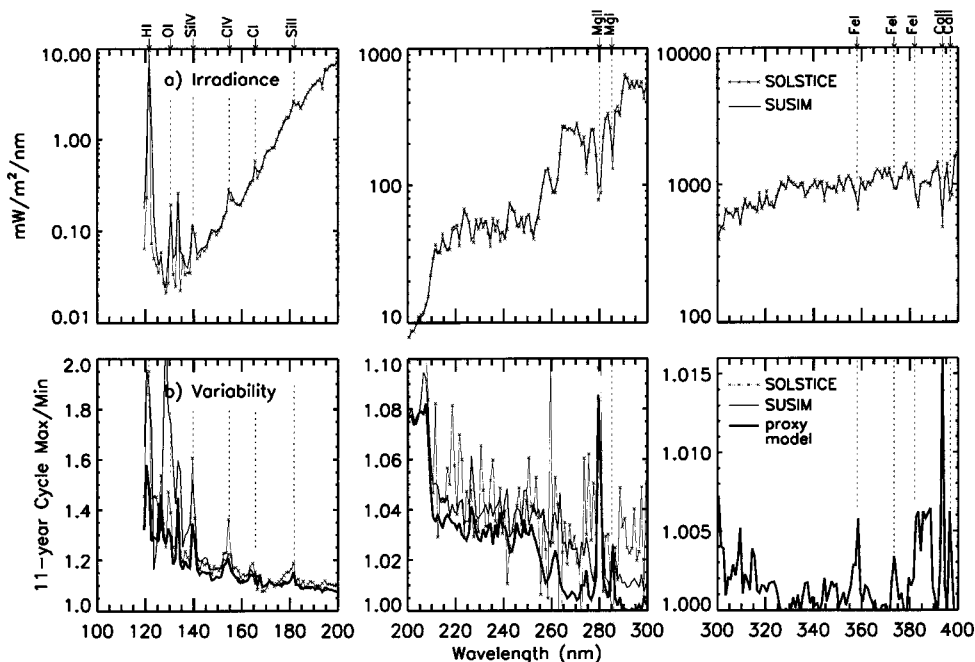


Figure 12. (top) Comparison of the SOLSTICE (crosses) and SUSIM (thin line) solar spectra averaged for February 1992, a period of high solar activity. (bottom) Ratios of the February 1992 spectrum to an average spectrum for March 1996, a period of low activity, recorded by SOLSTICE (crosses) and SUSIM (thin line). Compared with these ratios are estimates from an empirical model [Lean et al., 1997] based on rotational scaling of SOLSTICE spectra with the Mg index and UV sunspot-blocking proxies (solid line). At wavelengths from 160 to 290 nm, the measurements and the model generally agree to within the $\pm 1\%$ long-term precision of the UARS solar monitoring. At wavelengths longward of 290 nm the $\pm 1\%$ uncertainty in the data precludes observational validation of the factor of 2 or more smaller cycle variability that the model estimates.

series since 1976, integrated over geophysically relevant wavelengths. The reconstructions are determined from regression analysis of rotationally modulated SOLSTICE spectra with UV sunspot darkening and Mg index facular brightening proxies [Lean et al., 1997]. Also reconstructed in Figure 13 from sunspot and facular parameterizations of ACRIM I data, verified with ACRIM II measurements [Lean et al., 1995], is the total irradiance time series. The stratosphere and troposphere

absorb UV radiation in the 200- to 295- and 295- to 310-nm bands, respectively. Together, these two UV energy bands change by 0.17 W m^{-2} during the 11-year cycle, contributing about 13% of the total irradiance variability.

SOLSTICE's superior short-term precision permits detection and parameterizations of sunspot darkening and facular brightening influences at wavelengths greater than 300 nm, which were essentially unknown

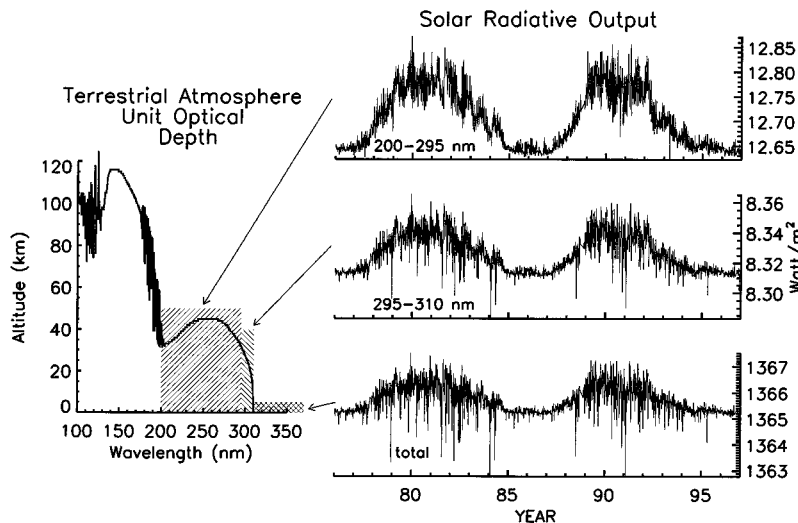


Figure 13. (left) Deposition altitudes of solar radiation energy, given by the altitude of unit optical depth for an overhead Sun [Meier, 1991]. Radiation in the broad wavelength bands (top) 200–295 nm, (middle right) 295–310 nm, and (bottom) total, reconstructed from proxy parameterizations of UARS solar data. These energy bands are absorbed primarily in the stratosphere, in the troposphere and near the Earth's surface, respectively.

prior to UARS. Figure 12 shows that the net effect of these competing influences during the 11-year activity cycle produces variabilities of a few tenths of a percent, predominantly in the cores of absorption lines [Lean et al., 1997]. UARS solar monitoring with $\pm 1\%$ long-term precision cannot verify these cycle amplitudes, but variabilities of a few tenths of a percent at near-UV wavelengths are consistent with the 0.1% total irradiance activity cycle, which is dominated by less variable radiation at longer, visible wavelengths [Foukal and Lean, 1988].

Scalings of rotationally modulated UARS 100- to 300-nm spectra using the Mg index [Heath and Schlesinger, 1986] or He EW [Harvey and Livingston, 1994] facular proxies predict 11-year cycle variations, shown in Figure 12, of 3% at 250 nm, 8% at 200 nm, and 20% in the UV 135-nm continuum radiation. At 200 nm, direct measurements by both the SOLSTICE and SUSIM indicate comparable cycle amplitudes, validating the use of this scaling approach [Chandra et al., 1995]. Between 210 and 260 nm the rotational scalings of the Mg index proxy predict solar cycle changes in general agreement with the SOLSTICE version 9 and SUSIM version 19 data to within their $\pm 1\%$ long-term precision uncertainties. However, Figure 12 illustrates that at wavelengths less than 160 nm, the reconstructions generally underestimate the long-term changes recorded by the UARS solar monitoring, especially in the cores of emission lines. Differences between the SOLSTICE (version 9) and SUSIM (version 19) long-term trends also increase, with SOLSTICE indicating smaller long-term irradiance changes than SUSIM. The largest discrepancies occur at the shortest wavelengths: SOLSTICE and SUSIM report long-term changes in the HI Lyman alpha irradiance of about 95%, whereas rotational scaling of the Mg index predicts an 11-year cycle of 60%.

The relationships established between UARS solar irradiance and solar activity proxies allow comparisons with prior irradiance measurements. Solar 200-nm irradiance measured by the Solar Mesosphere Explorer (SME) during cycles 21 and 22 [Rottman, 1988], adjusted upward by 7.3%, and by SOLSTICE during the descending phase of cycle 22 provide a mutually consistent record of an 8% 11-year cycle, in good agreement with proxy models. In contrast, inconsistencies are present in the composite HI Lyman alpha irradiance database. Aside from uncertainties traceable to absolute radiometric calibrations, there are discrepancies in variability amplitudes and in empirical relationships with standard solar activity proxies. SME Lyman alpha irradiance measurements indicate an 11-year solar cycle amplitude of about 50%, in better agreement with the proxy models than with the UARS measurements. If these differences are real, then the relationship of the Sun's HI Lyman alpha emission with solar activity is apparently nonlinear and unpredictable from one cycle to the next. An alternative explanation is the presence of unidentified instru-

mental drifts in the database, implied by comparisons with independent Pioneer Venus airglow signals [Tobiska et al., 1997]. Resolution awaits additional UARS monitoring during the increasing solar activity in cycle 23, subsequent processings of the UARS data with refined instrument sensitivity tracking algorithms, and more detailed understanding of the solar origins of the Lyman alpha irradiance variations.

In conclusion, solar radiometers on UARS have tracked the Sun's UV and total radiative output during the descending phase of solar cycle 22 and are presently recording low levels of radiative output during the present solar cycle activity minimum. Extensive preflight characterization and calibration, in-flight sensitivity tracking, and comparison with other measurements validate the UARS solar UV spectral irradiance measurements as the most accurate and precise made to date. These data offer a unique opportunity to study critical connections between the output of energy from the Sun and the Earth's atmosphere.

10. CONCLUSIONS

The UARS is providing a wealth of new information on the Earth's middle and upper atmosphere and on the radiative output of the Sun. As of this writing, nearly 400 refereed scientific papers have utilized results from UARS. In every sense, the mission has been and continues to be a success.

At the present time, the UARS is still obtaining data from several of its instruments. While some problems with the spacecraft have developed, we expect the UARS to continue to operate for several more years. As the length of the UARS data set continues to grow, an emphasis will be placed on quantitative determination of the trends in many of the measured parameters, including solar measurements, as well as on a continuation of monitoring of global ozone loss. We fully expect future analyses of these data to be as intriguing and illuminating as results from the first 5 years of the UARS mission have been. Finally, measurements from the UARS provide a solid foundation on which to interpret measurements from next-generation instruments. These instruments will be called upon to address current and future scientific questions regarding the abundance of lower stratospheric ozone loss and the climatic impact of mankind on the Earth, as well as issues that have not yet even been identified.

APPENDIX

With few exceptions, the UARS data are publicly available at the NASA Goddard Space Flight Center Distributed Active Archive Center (GSFC DAAC). These data are available via ftp:

telnet daac.gsfc.nasa.gov

login: daacims

password: gsfcdaac

The first 3 years of UARS data (September 1991 to September 1994) are also available on CD-ROM. Information about the UARS CD-ROMs is available via e-mail at “uarscd@cdhf6.gsfc.nasa.gov” or by writing, UARS CDHF, Building 23, 4th Floor, Room N406A, Mail Stop 64, NASA Goddard Space Flight Center, Greenbelt, MD 20771.

ACKNOWLEDGMENTS. We thank G. L. Manney for her important contributions to section 6, and C. J. Praderas, A. E. Roche, and P. A. Newman for help with Figures 1, 11, and 12, respectively. Many useful comments were provided by A. J. Dessler, E. E. Remsberg, R. S. Stolarski, and P. J. Crutzen. This work was supported in part by several NASA UARS Guest Investigator Program Grants (S.T.M., J.L.L.), NASA grant NAG-5-3188 (J.R.H.), and the UARS Project Office (A.E.D., M.R.S., A.R.D., C.H.J.). The National Center for Atmospheric Research (NCAR) is sponsored by the National Science Foundation.

Michael T. Coffey was the Editor responsible for this paper. He thanks David Rusch and William Randall for their technical reviews, and Bridget R. Scanlon for her cross-disciplinary review.

REFERENCES

- Abreu, V. J., A. Bucholtz, P. B. Hays, D. Ortland, W. R. Skinner, and J. H. Yee, Absorption and emission line shapes in the O₂ atmospheric bands: Theoretical model and limb viewing simulations, *Appl. Opt.*, **28**, 2128–2137, 1989.
- Asrar, G., and D. J. Dokken (Eds.), EOS Earth Observing System reference handbook, Earth Sci. Support Off. Doc. Resour. Facil., NASA, Washington, D. C., 1993.
- Avallone, L. M., and M. J. Prather, Photochemical evolution of ozone in the lower tropical stratosphere, *J. Geophys. Res.*, **101**, 1457–1461, 1996.
- Balachandran, N. K., and D. Rind, Modeling the effects of UV variability and the QBO on the troposphere-stratosphere system, 1, The middle atmosphere, *J. Clim.*, **8**, 2058–2079, 1995.
- Brueckner, G. E., K. L. Edlow, L. E. Floyd, J. L. Lean, and M. E. VanHoosier, The solar ultraviolet spectral irradiance monitor (SUSIM) experiment on board the Upper Atmosphere Research Satellite, *J. Geophys. Res.*, **98**, 695–10,711, 1993.
- Brühl, C., et al., HALOE ozone channel validation, *J. Geophys. Res.*, **101**, 10,217–10,240, 1996.
- Burrage, M. D., N. Arvin, W. R. Skinner, and P. B. Hays, Observations of the O₂ atmospheric band nightglow by the High Resolution Doppler Imager, *J. Geophys. Res.*, **99**, 15,017–15,023, 1994.
- Burrage, M. D., D. L. Wu, W. R. Skinner, D. A. Ortland, and P. B. Hays, Latitude and seasonal dependence of the semi-diurnal tide observed by HRDI, *J. Geophys. Res.*, **100**, 11,313–11,321, 1995a.
- Burrage, M. D., M. E. Hagan, W. R. Skinner, D. L. Wu, and P. B. Hays, Long-term variability in the solar diurnal tide observed by HRDI and simulated by the GSWM, *Geophys. Res. Lett.*, **22**, 2641–2644, 1995b.
- Burrage, M. D., R. A. Vincent, H. G. Mayr, W. R. Skinner, N. F. Arnold, and P. B. Hays, Long-term variability in the equatorial middle atmosphere zonal wind, *J. Geophys. Res.*, **101**, 12,847–12,854, 1996.
- Cebula, R. P., M. T. Deland, and B. M. Schlessinger, Estimates of solar variability using the backscatter ultraviolet (SBUV) 2 Mg II index from the NOAA 9 satellite, *J. Geophys. Res.*, **97**, 11,613–11,620, 1992.
- Chandra, S., J. L. Lean, O. R. White, D. K. Prinz, G. R. Rottman, and G. E. Brueckner, Solar UV irradiance variability during the declining phase of solar cycle 22, *Geophys. Res. Lett.*, **22**, 2481–2484, 1995.
- Coffey, M. T., Observations of the impact of volcanic activity on stratospheric chemistry, *J. Geophys. Res.*, **101**, 6767–6780, 1996.
- Crutzen, P. J., J.-U. Grooss, C. Brühl, R. Müller, and J. M. Russell III, A reevaluation of the ozone budget with HALOE UARS data: No evidence for the ozone deficit, *Science*, **268**, 705–708, 1995.
- Crutzen, P. J., and U. Schmailzl, Chemical budgets of the stratosphere, *Planet. Space Sci.*, **31**, 1009–1032, 1983.
- DeMore, W. B., S. P. Sander, D. M. Golden, R. F. Hampson, M. J. Kurylo, C. J. Howard, A. R. Ravishankara, C. E. Kolb, and M. J. Molina, Chemical kinetics and photochemical data for use in stratospheric modeling, *JPL Publ.*, **94-26**, 1994.
- Deshler, T., B. J. Johnson, and W. B. Rozier, Balloonborne measurements of Pinatubo aerosol during 1991 and 1992 at 41°N: Vertical profiles, size distributions and volatility, *Geophys. Res. Lett.*, **20**, 1435–1438, 1993.
- Dessler, A. E., et al., Balloon-borne measurements of ClO, NO, and O₃ in a volcanic cloud: An analysis of heterogeneous chemistry between 20 and 30 km, *Geophys. Res. Lett.*, **20**, 2527–2530, 1993.
- Dessler, A. E., E. M. Weinstock, E. J. Hints, J. G. Anderson, C. R. Webster, R. D. May, J. W. Elkins, and G. S. Dutton, An examination of the total hydrogen budget of the lower stratosphere, *Geophys. Res. Lett.*, **21**, 2563–2566, 1994.
- Dessler, A. E., et al., Correlated observations of HCl and ClONO₂ from UARS and implications for stratospheric chlorine partitioning, *Geophys. Res. Lett.*, **22**, 1721–1724, 1995.
- Dessler, A. E., S. R. Kawa, D. B. Considine, J. W. Waters, L. Froidevaux, and J. B. Kumer, UARS measurements of ClO and NO₂ at 40 and 46 km and implications for the model “ozone deficit,” *Geophys. Res. Lett.*, **23**, 339–342, 1996a.
- Dessler, A. E., S. R. Kawa, A. R. Douglass, D. B. Considine, J. B. Kumer, A. E. Roche, J. L. Mergenthaler, J. W. Waters, J. M. Russell III, and J. C. Gille, A test of the partitioning between ClO and ClONO₂ using simultaneous UARS measurements of ClO, NO₂, and ClONO₂, *J. Geophys. Res.*, **101**, 12,515–12,521, 1996b.
- Eluszkiewicz, J., and M. Allen, A global analysis of the ozone deficit in the upper stratosphere and lower mesosphere, *J. Geophys. Res.*, **98**, 1069–1082, 1993.
- Fahey, D. W., et al., In situ measurements constraining the role of sulphate aerosols in mid-latitude ozone depletion, *Nature*, **363**, 509–514, 1993.
- Finkbeiner, M., J. N. Crowley, O. Horie, R. Müller, G. K. Moortgat, and P. J. Crutzen, The reaction between HO₂ and ClO: Product formation between 210 K and 300 K, *J. Phys. Chem.*, **99**, 16,264–16,275, 1995.
- Foukal, P., and J. Lean, Magnetic modulation of solar luminosity by photospheric activity, *Astrophys. J.*, **328**, 347–357, 1988.
- Fröhlich, C., Irradiance observations of the Sun, in *The Sun as a Variable Star*, edited by J. M. Pap et al., *Int. Astron. Union Colloq.*, **143**, 28–36, 1994.
- Froidevaux, L., M. Allen, and Y. L. Yung, A critical analysis of ClO and O₃ in the midlatitude stratosphere, *J. Geophys. Res.*, **90**, 12,999–13,029, 1985.

- Froidevaux, L., J. W. Waters, W. G. Read, L. S. Elson, D. A. Flower, and R. F. Jarnot, Global ozone observations from UARS MLS: An overview of zonal mean results, *J. Atmos. Sci.*, *51*, 2846–2866, 1994.
- Geller, M. A., V. Yudin, A. R. Douglas, J. W. Waters, L. S. Elson, A. E. Roche, and J. M. Russell III, UARS PSC, ClONO₂, HCl, and ClO measurements in early winter: Additional verification of the paradigm for chlorine activation, *Geophys. Res. Lett.*, *22*, 2937–2940, 1995.
- Gille, J. C., et al., Accuracy and precision of Cryogenic Limb Array Etalon Spectrometer (CLAES) temperature retrievals, *J. Geophys. Res.*, *101*, 9583–9601, 1996.
- Gordley, L. L., et al., Validation of nitric oxide and nitrogen dioxide measurements made by HALOE for UARS platform, *J. Geophys. Res.*, *101*, 10,241–10,266, 1996.
- Grainger, R. G., A. Lambert, F. W. Taylor, J. J. Remedios, C. D. Rodgers, M. Corney, and B. J. Kerridge, Infrared absorption by volcanic stratospheric aerosols observed by ISAMS, *Geophys. Res. Lett.*, *20*, 1283–1286, 1993.
- Grainger, R. G., A. Lambert, C. D. Rodgers, F. W. Taylor, and T. Deshler, Stratospheric aerosol effective radius, surface, and volume estimated from infrared measurements, *J. Geophys. Res.*, *100*, 16,507–16,518, 1995.
- Granier, C., and G. Brasseur, Impact of heterogeneous chemistry on model predictions of ozone changes, *J. Geophys. Res.*, *97*, 18,015–18,033, 1992.
- Hagan, M. E., J. M. Forbes, and F. Vial, On modeling migrating solar tides, *Geophys. Res. Lett.*, *22*, 893–896, 1995.
- Hansen, J., et al., Forcings and chaos in interannual to decadal climate change, *J. Geophys. Res.*, *102*, 25,679–25,720, 1997.
- Hanson, D. R., A. R. Ravishankara, and S. Solomon, Heterogeneous reactions in sulfuric acid aerosols: A framework for model calculations, *J. Geophys. Res.*, *99*, 3615–3629, 1994.
- Harries, J. E., J. M. Russell III, A. F. Tuck, L. L. Gordley, P. Purcell, K. Stone, R. M. Bevilacqua, M. Gunson, G. Nedoluha, and W. A. Traub, Validation of measurements of water vapor from the Halogen Occultation Experiment (HALOE), *J. Geophys. Res.*, *101*, 10,205–10,216, 1996.
- Hartmann, D. L., B. R. Barkstrom, D. Crommelynek, P. Foukal, J. E. Hansen, J. Lean, R. B. Lee III, M. R. Schoeberl, and R. C. Willson, Total solar irradiance monitoring, *Earth Observer*, *5*, 23–27, 1993.
- Harvey, J. W., and W. C. Livingston, Variability of the solar He I 10830 Å triplet, in *Infrared Solar Physics*, edited by D. M. Rabin, J. T. Jefferies, and C. Lindsey, *Symp. 154, Int. Astron. Union*, 59–64, 1994.
- Hays, P. B., and D. L. Wu, Observations of the diurnal tide from space, *J. Atmos. Sci.*, *51*, 3077–3093, 1994.
- Hays, P. B., et al., Remote sensing of mesospheric winds with the High Resolution Doppler Imager, *Planet. Space Sci.*, *40*, 1599–1606, 1992.
- Hays, P. B., V. J. Abreu, M. E. Dobbs, D. A. Gell, H. J. Grassl, and W. R. Skinner, The High Resolution Doppler Imager on the Upper Atmosphere Research Satellite, *J. Geophys. Res.*, *98*, 10,713–10,723, 1993.
- Heath, D. F., and B. M. Schlessinger, The Mg 280-nm doublet as a monitor of changes in solar ultraviolet irradiance, *J. Geophys. Res.*, *91*, 8672–8682, 1986.
- Hervig, M. E., J. M. Russell III, L. L. Gordley, J. H. Park, S. R. Drayson, and T. Deshler, Validation of aerosol measurements from the Halogen Occultation Experiment, *J. Geophys. Res.*, *101*, 10,267–10,275, 1996.
- Hinteregger, H. E., K. Fukui, and B. G. Gilson, Observational, reference and model data on solar EUV, from measurements on AE-E, *Geophys. Res. Lett.*, *8*, 1147–1150, 1981.
- Hofmann, D. J., and S. J. Oltmans, Anomalous Antarctic ozone during 1992: Evidence for Pinatubo volcanic aerosol effects, *J. Geophys. Res.*, *98*, 18,555–18,561, 1993.
- Hofmann, D. J., S. J. Oltmans, J. A. Lathrop, J. M. Harris, and H. Vömel, Record low ozone at the South Pole in the spring of 1993, *Geophys. Res. Lett.*, *21*, 421–424, 1994.
- Holton, J. R., P. H. Haynes, M. E. McIntyre, A. R. Douglass, R. B. Rood, and L. Pfister, Stratosphere-troposphere exchange, *Rev. Geophys.*, *33*, 403–439, 1995.
- Hoyt, D. V., H. L. Kyle, J. R. Hickey, and R. H. Maschhoff, The Nimbus 7 solar total irradiance: A new algorithm for its derivation, *J. Geophys. Res.*, *97*, 51–63, 1992.
- Jackman, C. H., R. S. Stolarski, and J. A. Kaye, Two-dimensional monthly average ozone balance from Limb Infrared Monitor of the Stratosphere and Stratospheric and Mesospheric Sounder data, *J. Geophys. Res.*, *91*, 1103–1116, 1986.
- Johannesson, A., W. Marquette, and H. Zirin, Reproduction of the Lyman α irradiance variability from analysis of full-disk images in the Ca II K-line, *Sol. Phys.*, *161*, 201–204, 1995.
- Kinnison, D. E., K. E. Grant, P. S. Connell, D. A. Rotman, and D. J. Wuebbles, The chemical and radiative effects of the Mount Pinatubo eruption, *J. Geophys. Res.*, *99*, 25,705–25,732, 1994.
- Kyle, H. L., D. V. Hoyt, and J. R. Hickey, A review of the Nimbus-7 ERB solar data set, *Solar Phys.*, *152*, 9–12, 1994.
- Lambert, A., R. G. Grainger, J. J. Remedios, C. D. Rodgers, M. Corney, and F. W. Taylor, Measurements of the evolution of the Mt. Pinatubo aerosol cloud by ISAMS, *Geophys. Res. Lett.*, *20*, 1287–1290, 1993.
- Lambert, A., R. G. Grainger, J. J. Remedios, W. J. Reburn, C. D. Rodgers, F. W. Taylor, A. E. Roche, J. B. Kumer, S. T. Massie, and T. Deshler, Validation of aerosol measurements from the Improved Stratospheric and Mesospheric Sounder, *J. Geophys. Res.*, *101*, 9811–9830, 1996a.
- Lambert, A., R. G. Grainger, H. L. Rogers, W. A. Norton, C. D. Rodgers, and F. W. Taylor, The H₂SO₄ component of stratospheric aerosols derived from satellite infrared extinction measurements: Applications to stratospheric transport studies, *Geophys. Res. Lett.*, *23*, 2219–2222, 1996b.
- Latimer, D., P. McLoughlin, and J. Wiesenfeld, Detailed balance limits the rate of odd oxygen production in the reaction of vibrationally excited oxygen with O₂, *Geophys. Res. Lett.*, *23*, 1083–1086, 1996.
- Lean, J., Variations in the Sun's radiative output, *Rev. Geophys.*, *29*, 505–535, 1991.
- Lean, J., M. VanHoosier, G. Brueckner, D. Prinz, L. Floyd, and K. Edlow, SUSIM/UARS observations of the 120 to 300 nm flux variations during the maximum of the solar cycle: Inferences for the 11-year cycle, *Geophys. Res. Lett.*, *19*, 2203–2206, 1992.
- Lean, J., J. Beer, and R. Bradley, Reconstruction of solar irradiance since 1610: Implications for climate change, *Geophys. Res. Lett.*, *22*, 3195–3198, 1995.
- Lean, J. L., G. J. Rottman, H. L. Kyle, T. N. Woods, J. R. Hickey, and L. C. Puga, Detection and parameterization of variations in solar mid- and near-ultraviolet radiation (200–400 nm), *J. Geophys. Res.*, *102*, 29,939–29,956, 1997.
- Lee, R. B., III, M. A. Gibson, R. S. Wilson, and S. Thomas, Long-term total solar irradiance variability during sunspot cycle 22, *J. Geophys. Res.*, *100*, 1667–1675, 1995.
- Lieberman, R. S., Long-term variations in zonal winds and (1,1) driving in the equatorial lower thermosphere, *J. Atmos. Sol. Terr. Phys.*, *59*, 1483–1490, 1997.
- Lieberman, R. S., and P. B. Hays, An estimate of the momentum deposition in the lower thermosphere by the observed diurnal tide, *J. Atmos. Sci.*, *51*, 3094–3105, 1994.
- Lieberman, R. S., M. D. Burrage, D. A. Gell, P. B. Hays, A. R. Marshall, D. A. Ortland, W. R. Skinner, D. L. Wu, R. A. Vincent, and S. J. Franke, Zonal mean winds in the equatorial mesosphere and lower thermosphere observed by the High Resolution Doppler Imager, *Geophys. Res. Lett.*, *20*, 2849–2852, 1993.

- Lipson, J. B., M. J. Elrod, T. W. Beiderhase, L. T. Molina, and M. J. Molina, Temperature dependence of the rate constant and branching ratio for the OH + ClO reaction, *J. Chem. Soc. Faraday Trans.*, 93, 2665–2673, 1997.
- London, J., G. J. Rottman, T. N. Woods, and F. Wu, Time variations of solar UV irradiance as measured by the SOLSTICE (UARS) instrument, *Geophys. Res. Lett.*, 20, 1315–1318, 1993.
- Manney, G. L., R. W. Zurek, A. O'Neill, and R. Swinbank, On the motion of air through the stratospheric polar vortex, *J. Atmos. Sci.*, 51, 2973–2994, 1994.
- Manney, G. L., R. W. Zurek, L. Froidevaux, J. W. Waters, A. O'Neill, and R. Swinbank, Lagrangian transport calculations using UARS data, II, Ozone, *J. Atmos. Sci.*, 52, 3069–3081, 1995a.
- Manney, G. L., R. W. Zurek, L. Froidevaux, and J. W. Waters, Evidence for Arctic ozone depletion in late February and early March 1994, *Geophys. Res. Lett.*, 22, 2941–2944, 1995b.
- Manney, G. L., et al., Lagrangian transport calculations using UARS data, I, Passive tracers, *J. Atmos. Sci.*, 52, 3049–3068, 1995c.
- Manney, G. L., M. L. Santee, L. Froidevaux, J. W. Waters, and R. W. Zurek, Polar vortex conditions during the 1995–96 Arctic winter: Meteorology and MLS ozone, *Geophys. Res. Lett.*, 23, 3203–3206, 1996a.
- Manney, G. L., L. Froidevaux, J. W. Waters, M. L. Santee, W. G. Read, D. A. Flower, R. F. Jarnot, and R. W. Zurek, Arctic ozone depletion observed by UARS MLS during the 1994–95 winter, *Geophys. Res. Lett.*, 23, 85–88, 1996b.
- Massie, S. T., P. L. Bailey, J. C. Gille, E. C. Lee, J. L. Mergenthaler, A. E. Roche, J. B. Kumer, E. F. Fishbein, J. W. Waters, and W. A. Lahoz, Spectral signatures of polar stratospheric clouds and sulfate aerosol, *J. Atmos. Sci.*, 51, 3027–3044, 1994.
- Massie, S. T., et al., Validation studies using multiwavelength Cryogenic Limb Array Etalon Spectrometer (CLAES) observations of stratospheric aerosol, *J. Geophys. Res.*, 101, 9757–9773, 1996a.
- Massie, S. T., T. Deshler, G. E. Thomas, J. L. Mergenthaler, and J. M. Russell III, Evolution of the infrared properties of the Mount Pinatubo aerosol cloud over Laramie, Wyoming, *J. Geophys. Res.*, 101, 23,007–23,019, 1996b.
- McCormick, M. P., and R. E. Veiga, SAGE II measurements of early Pinatubo aerosols, *Geophys. Res. Lett.*, 19, 155–158, 1992.
- McIntyre, M. E., Atmospheric dynamics: Some fundamentals, with observational implications, in *The Use of EOS for Studies of Atmospheric Physics*, edited by J. C. Gille and G. Visconti, pp. 313–386, North-Holland, New York, 1992.
- McIntyre, M. E., and T. N. Palmer, The 'surf zone' in the stratosphere, *J. Atmos. Terr. Phys.*, 46, 825–849, 1984.
- McLandress, C., Y. Rochon, G. G. Shepherd, B. H. Solheim, G. Thuillier, and F. Vial, The meridional wind component of the thermospheric tide observed by WINDII on UARS, *Geophys. Res. Lett.*, 21, 2417–2420, 1994.
- McLandress, C., G. G. Shepherd, and B. H. Solheim, Satellite observations of thermospheric tides: Results from the wind imaging interferometer on UARS, *J. Geophys. Res.*, 101, 4093–4114, 1996a.
- McLandress, C., G. G. Shepherd, B. H. Solheim, M. D. Burrage, P. B. Hays, and W. R. Skinner, Combined mesosphere/thermosphere winds using WINDII and HRDI data from the Upper Atmosphere Research Satellite, *J. Geophys. Res.*, 101, 10,441–10,453, 1996b.
- Mecherikunnel, A. T., A comparison of solar total irradiance observations from spacecraft: 1985–1992, *Sol. Phys.*, 155, 211–221, 1994.
- Meier, R. R., Ultraviolet spectroscopy and remote sensing of the upper atmosphere, *Space Sci. Rev.*, 58, 1–185, 1991.
- Mengel, J. H., H. G. Mayr, K. L. Chan, C. O. Hines, C. A. Reddy, N. F. Arnold, and H. S. Porter, Equatorial oscillations in the middle atmosphere generated by small scale gravity waves, *Geophys. Res. Lett.*, 22, 3027–3030, 1995.
- Mergenthaler, J. L., J. B. Kumer, and A. E. Roche, CLAES observations of Mt. Pinatubo stratospheric aerosol, *Geophys. Res. Lett.*, 22, 3497–3500, 1995.
- Mergenthaler, J. L., et al., Validation of CLAES ClONO₂ measurements, *J. Geophys. Res.*, 101, 9603–9620, 1996.
- Michelsen, H. A., R. J. Salawitch, P. O. Wennberg, and J. G. Anderson, Production of O(¹D) from photolysis of O₃, *Geophys. Res. Lett.*, 21, 2227–2230, 1994.
- Miller, R. L., A. G. Suits, P. L. Houston, R. Toumi, J. A. Mack, and A. M. Wodtke, The "ozone deficit" problem: O₂(X, v >= 26) + O(³P) from 226-nm ozone photodissociation, *Science*, 265, 1831–1838, 1994.
- Minschwaner, K., R. J. Salawitch, and M. B. McElroy, Absorption of solar radiation by O₂: Implications for O₃ and lifetimes of N₂O, CFCl₃, and CF₂Cl₂, *J. Geophys. Res.*, 98, 10,543–10,561, 1993.
- Minschwaner, K., A. E. Dessler, J. W. Elkins, C. M. Volk, D. W. Fahey, M. Loewenstein, J. R. Podolske, A. E. Roche, and K. R. Chan, Bulk properties of isentropic mixing into the tropics in the lower stratosphere, *J. Geophys. Res.*, 101, 9433–9439, 1996.
- Morris, G. A., et al., Trajectory mapping and applications to data from the Upper Atmosphere Research Satellite, *J. Geophys. Res.*, 100, 16,491–16,505, 1995.
- Morton, Y. T., R. S. Lieberman, P. B. Hays, D. A. Ortland, A. R. Marshall, D. Wu, W. R. Skinner, M. D. Burrage, D. A. Gell, and J.-H. Yee, Global mesospheric tidal winds observed by the High Resolution Doppler Imager on board the Upper Atmosphere Research Satellite, *Geophys. Res. Lett.*, 20, 1263–1266, 1993.
- Mote, P. W., K. H. Rosenlof, M. E. McIntyre, E. S. Carr, J. C. Gille, J. R. Holton, J. S. Kinnarsley, H. C. Pumphrey, J. M. Russell III, and J. W. Waters, An atmospheric tape recorder: The imprint of tropical tropopause temperatures on stratospheric water vapor, *J. Geophys. Res.*, 101, 3989–4006, 1996.
- Müller, R., P. J. Crutzen, J.-U. Grooss, C. Bruhl, J. M. Russell III, and A. F. Tuck, Chlorine activation and ozone depletion in the Arctic vortex: Observations by the Halogen Occultation Experiment on the Upper Atmosphere Research Satellite, *J. Geophys. Res.*, 101, 12,531–12,554, 1996.
- Natarajan, M., and L. B. Callis, Stratospheric Photochemical Studies With Atmospheric Trace Molecule Spectroscopy (ATMOS) Measurements, *J. Geophys. Res.*, 96, 9361–9370, 1991.
- Nightingale, R. W., et al., Global CF₂Cl₂ measurements by UARS Cryogenic Limb Array Etalon Spectrometer: Validation by correlative data and a model, *J. Geophys. Res.*, 101, 9711–9736, 1996.
- Norton, W. A., Breaking Rossby waves in a model stratosphere diagnosed by a vortex-following coordinate system and a technique for advecting material contours, *J. Atmos. Sci.*, 51, 654–673, 1994.
- Plumb, R. A., and M. K. W. Ko, Interrelationships between mixing ratios of long-lived stratospheric constituents, *J. Geophys. Res.*, 97, 10,145–10,156, 1992.
- Randel, W. J., J. C. Gille, A. E. Roche, J. B. Kumer, J. L. Mergenthaler, J. W. Waters, E. F. Fishbein, and W. A. Lahoz, Stratospheric transport from the tropics to middle latitudes by planetary-wave mixing, *Nature*, 365, 533–535, 1993.
- Read, W. G., L. Froidevaux, and J. W. Waters, Microwave Limb Sounder measurements of stratospheric SO₂ from the Mt. Pinatubo volcano, *Geophys. Res. Lett.*, 20, 1299–1302, 1993.
- Reber, C. A., The Upper Atmosphere Research Satellite, *Geophys. Res. Lett.*, 20, 1215–1218, 1993.
- Rinsland, C. P., G. K. Yue, M. B. Gunson, R. Zander, and

- M. C. Abrams, Mid-infrared extinction by sulfate aerosols from the Mt. Pinatubo eruption, *J. Quant. Spectrosc. Radiat. Transfer*, **52**, 241–252, 1994.
- Rottman, G. J., Observations of solar UV and EUV variability, *Adv. Space Res.*, **8**(7), 53–66, 1988.
- Rottman, G. J., T. N. Woods, and T. P. Sparr, Solar-Stellar Irradiance Comparison Experiment, 1, Instrument design and operation, *J. Geophys. Res.*, **98**, 10,667–10,677, 1993.
- Russell, J. M., III, et al., Validation of hydrogen chloride measurements made by the Halogen Occultation Experiment from the UARS platform, *J. Geophys. Res.*, **101**, 10,151–10,162, 1996a.
- Russell, J. M., III, M. Luo, R. J. Cicerone, and L. E. Deaver, Satellite confirmation of the dominance of chlorofluorocarbons in the global stratospheric chlorine budget, *Nature*, **379**, 526–529, 1996.
- Salawitch, R. J., et al., The distribution of hydrogen, nitrogen, and chlorine radicals in the lower stratosphere: Implications for changes in O₃ due to emission of NO_y from supersonic aircraft, *Geophys. Res. Lett.*, **21**, 2547–2550, 1994.
- Santee, M. L., G. L. Manney, W. G. Read, L. Froidevaux, and J. W. Waters, Polar vortex conditions during the 1995–96 Arctic winter: MLS ClO and HNO₃, *Geophys. Res. Lett.*, **23**, 3207–3210, 1996.
- Schoeberl, M. R., M. H. Proffitt, K. K. Kelly, L. R. Lait, P. A. Newman, J. E. Rosenfield, M. Loewenstein, J. R. Poddsk, S. E. Strahan, and K. R. Chan, Stratospheric constituent trends from ER-2 profile data, *Geophys. Res. Lett.*, **17**, 469–472, 1990.
- Schoeberl, M. R., R. S. Stolarski, A. R. Douglass, P. A. Newman, L. R. Lait, J. W. Waters, L. Froidevaux, and W. G. Read, MLS ClO observations and Arctic polar vortex temperatures, *Geophys. Res. Lett.*, **20**, 2861–2864, 1993.
- Schoeberl, M. R., A. R. Douglass, R. Kawa, A. E. Dessler, P. A. Newman, R. S. Stolarski, A. E. Roche, J. W. Waters, and J. M. Russell III, Development of the Antarctic ozone hole, *J. Geophys. Res.*, **101**, 20,909–20,924, 1996.
- Shepherd, G. G., et al., WINDII, the Wind Imaging Interferometer on the Upper Atmosphere Research Satellite, *J. Geophys. Res.*, **98**, 10,725–10,750, 1993.
- Shepherd, G. G., C. McLandress, and B. H. Solheim, Tidal influence on O(¹S) airglow emission rate distributions at the geographic equator as observed by WINDII, *Geophys. Res. Lett.*, **22**, 275–278, 1995.
- Siskind, D. E., B. J. Connor, R. S. Eckman, E. E. Remsburg, J. J. Tsou, and A. Parrish, An intercomparison of model ozone deficits in the upper stratosphere and mesosphere from two data sets, *J. Geophys. Res.*, **100**, 11,191–11,201, 1995.
- Slanger, T. G., L. E. Jusinski, G. Black, and G. E. Gadd, A new laboratory source of ozone and its potential atmospheric implications, *Science*, **241**, 945–950, 1988.
- Stolarski, R. S., and R. J. Cicerone, Stratospheric chlorine: A possible sink for ozone, *Can. J. Chem.*, **52**, 1610–1615, 1974.
- Sutton, R. T., H. MacLean, R. Swinbank, A. O'Neill, and F. W. Taylor, High-resolution stratospheric tracer fields estimated from satellite observations using Lagrangian trajectory calculations, *J. Atmos. Sci.*, **51**, 2995–3005, 1994.
- Tobiska, W. K., W. R. Pryor, and J. M. Ajello, Solar hydrogen Lyman- α variation during solar cycles 21 and 22, *Geophys. Res. Lett.*, **24**, 1123–1126, 1997.
- Toumi, R., An evaluation of autocatalytic ozone production from vibrationally excited oxygen in the middle atmosphere, *J. Atmos. Chem.*, **15**, 69–77, 1992.
- Trepte, C. R., and M. H. Hitchman, Tropical stratospheric circulation deduced from satellite aerosol data, *Nature*, **355**, 626–628, 1992.
- Volk, C. M., et al., Quantifying transport between the tropical and mid-latitude lower stratosphere, *Science*, **272**, 1763–1768, 1996.
- Waters, J. W., et al., Validation of UARS Microwave Limb Sounder ClO measurements, *J. Geophys. Res.*, **101**, 10,091–10,127, 1996.
- Willson, R. C., Active cavity radiometer type IV, *Appl. Opt.*, **18**, 179–188, 1979.
- Willson, R. C., Solar monitoring has a past and present: Does it have a future?, in *The Sun as a Variable Star*, edited by J. M. Pap et al., *IAU Colloq.* **143**, 4–10, 1994.
- Willson, R. C., and H. S. Hudson, A solar cycle of measured and modeled total irradiance, *Nature*, **351**, 42–44, 1991.
- Woods, T. N., G. J. Rottman, and G. Ucker, Solar-Stellar Irradiance Comparison Experiment, 2, Instrument calibration, *J. Geophys. Res.*, **98**, 10,679–10,694, 1993.
- Woods, T. N., et al., Validation of the UARS solar ultraviolet irradiances: Comparison with the ATLAS 1 and 2 measurements, *J. Geophys. Res.*, **101**, 9541–9569, 1996.
- World Meteorological Organization (WMO), The stratosphere 1981: Theory and measurements, *WMO Rep. 11*, Global Ozone Res. and Monit. Proj., Geneva, 1981.
- World Meteorological Organization (WMO), Scientific assessment of ozone depletion: 1991, *WMO Rep. 25*, Global Ozone Res. and Monit. Proj., Geneva, 1992.
- World Meteorological Organization (WMO), Scientific assessment of ozone depletion: 1994, *WMO Rep. 37*, Global Ozone Res. and Monit. Proj., Geneva, 1995.
- Young, R. E., H. Houben, and O. B. Toon, Radiatively forced dispersion of the Mt. Pinatubo volcanic cloud and induced temperature perturbations in the stratosphere during the first few months following the eruption, *Geophys. Res. Lett.*, **21**, 369–372, 1994.
- Yudin, V. A., M. A. Geller, B. V. Khattatov, A. R. Douglass, M. C. Cerniglia, J. W. Waters, L. S. Elson, A. E. Roche, and J. M. Russell III, A UARS study of lower stratospheric polar processing in the early stages of northern and southern winters, *J. Geophys. Res.*, **102**, 19,137–19,148, 1997.
- Yulaeva, E., J. R. Holton, and J. M. Wallace, On the cause of the annual cycle in tropical lower-stratospheric temperatures, *J. Atmos. Sci.*, **51**, 169–174, 1994.
- Zurek, R. W., G. L. Manney, A. J. Miller, M. E. Gelman, and R. Nagatani, Interannual variability of the north polar vortex in the lower stratosphere during the UARS mission, *Geophys. Res. Lett.*, **23**, 289–292, 1996.

M. D. Burrage, Space Physics Research Laboratory, Department of Atmospheric, Oceanic, and Space Sciences, University of Michigan, 2455 Hayward Drive, Ann Arbor, MI 48109. (e-mail: burrage@sprlj.sprl.umich.edu)

A. E. Dessler, Department of Meteorology, University of Maryland, College Park, MD 20742. (e-mail: dessler@atmos.umd.edu)

A. R. Douglass, C. H. Jackman, and M. R. Schoeberl, Laboratory for Atmospheres, Code 910, NASA Goddard Space Flight Center, Greenbelt, MD 20771. (e-mail: douglass@xena.gsfc.nasa.gov; jackman@welkin.span.nasa.gov; schom@zephyr.gsfc.nasa.gov)

J.-U. Grooss, Forschungszentrum Jülich, ICG-1, D-52425 Jülich, Germany. (e-mail: j.-u.grooss@fz-juelich.de)

J. R. Holton, Department of Atmospheric Sciences, University of Washington, Box 351640, Seattle, WA 98195. (e-mail: holton@atmos.washington.edu)

J. L. Lean, Naval Research Laboratory, Code 7673L, Washington, DC 20375. (e-mail: lean@demeter.nrl.navy.mil)

S. T. Massie, National Center for Atmospheric Research, P.O. Box 3000, Boulder, CO 80307 (e-mail: massie@ncar.ucar.edu)